Fizika Nizkikh Temperatur, 2003, v. 29, No. 3, p. 321–341

Ion desorption from molecules condensed at low temperature: A study with electron-ion coincidence spectroscopy combined with synchrotron radiation

(Review Article)

Kazuhiko Mase

Photon Factory, Institute of Materials Structure Science, High Energy Accelerator Research Organization, 1-1 Oho, Tsukuba 305-0801, Japan

Mitsuru Nagasono*

Institute for Molecular Science, Okazaki 444-8585, Japan

Shin-ichiro Tanaka**

Department of Physics, Graduate School of Science, Nagoya University Furo-cho, Chikusa-ku, Nagoya 464-8602, Japan

Tetsuji Sekitani

Department of Physical Science, Graduate School of Science Hiroshima University, Higashi-Hiroshima 739-8526, Japan

Shin-ichi Nagaoka

Chemistry Group, Department of Fundamental Material Science, Faculty of Science, Ehime University, Matsuyama 790-8577, Japan
E-mail: nagaoka@ehimegw.dpc.ehime-u.ac.jp

Received 24 May, 2002

This article reviews our recent work on photo-stimulated ion desorption (PSID) from molecules condensed at low temperature. We have used electron-ion coincidence (EICO) spectroscopy combined with synchrotron radiation. The history and present status of the EICO apparatus is described, as well as our recent investigations of condensed H_2O, NH_3, CH_3CN, and CF_3CH_3. Auger electron photoion coincidence (AEPICO) spectra of condensed H_2O at the O:1*s* ionization showed that H^+ desorption was stimulated by O:KVV Auger processes leading to two–hole states (normal-Auger stimulated ion desorption (ASID) mechanism). The driving forces for H^+ desorption were attributed to the electron missing in the O–H bonding orbitals and the effective hole-hole Coulomb repulsion. The normal ASID mechanism was also demonstrated for condensed NH_3. The H^+ desorption at the $4a_1 \leftarrow$ O(N):1*s* resonance of both condensed H_2O and condensed NH_3 was found to be greatly enhanced. Based on the AEPICO spectra the following four-step mechanism was proposed: (1) the $4a_1 \leftarrow 1s$ transition, (2) extension of the HO–H (H_2N–H) distance within the lifetime of the $(1s)^{-1}(4a_1)^1$ state, (3) spectator Auger transitions leading to $(\text{valence})^{-2}(4a_1)^1$

* Present address: Department of Materials Science and Engineering, Graduate School of Engineering, Kyoto University, Sakyo-ku, Kyoto 606-8501, Japan

** Present address: The Institute of Scientific and Industrial Research Osaka University, 8-1 Mihogaoka, Ibaraki 567-0047, Japan

states, and (4) H^+ desorption. The enhancement of the H^+ desorption yield was attributed to the repulsive potential surface of the $(1s)^{-1}(4a_1)^1$ state. At the $3p \leftarrow$ O:1*s* resonance of condensed H_2O, on the other hand, the H^+ yield was found to be decreased. The AEPICO spectra showed that the H^+ desorption was stimulated by spectator Auger transitions leading to $(\text{valence})^{-2}(3p)^1$ states. The decrease in the H^+ yield was attributed to a reduction in the effective hole-hole Coulomb repulsion due to shielding by the 3*p* electron. Photoelectron photoion coincidence (PEPICO) spectra of condensed H_2O showed that the core level of the surface H_2O responsible for the H^+ desorption was shifted by 0.7 eV from that of the bulk H_2O. The H^+ desorption from condensed CH_3CN was also investigated. In a study of condensed CF_3CH_3 using PEPICO spectroscopy, site-specific ion desorption was directly verified; that is, H^+ and CH_3^+ desorption was predominant for the C:1*s* photoionization at the -CH_3 site, while $C_2H_n^+$, $CFCH_m^+$, and CF_3^+ desorption was predominantly induced by the C:1*s* photoionization at the -CF_3 site. These investigations demonstrate that EICO spectroscopy combined with synchrotron radiation is a powerful tool for studying PSID of molecules condensed at low temperature.

PACS: 79.20.La, **07.81.+a**

Contents

1. Introduction

Photo-stimulated ion desorption (PSID) induced by core-electron excitations of atoms and molecules on surfaces is an active research field in surface science [1–6]. Detailed investigations of this topic have been very valuable for the following areas: (1) vacuum technology to suppress ion desorption induced by electron impact, (2) chemical reactions induced by high-energy particles on the inner walls of accelerators and fusion reactors, and (3) radiation damage of biomolecules and x-ray optics. In addition, PSID at low temperature seems to play important roles in the solar system [7], for example, in production of O_2 on icy satellites [8], as a substantial source of sodium in the lunar atmosphere [9], and in the formation of interstellar molecular hydrogen on the surfaces of cosmic dust grains [10,11].

In studies of PSID, the electron-ion coincidence (EICO) method is a very powerful tool because it can be used to measure ion desorption yields for core excitation and subsequent Auger transitions. Although excitations of surfaces by x-ray-induced electrons (photoelectrons, Auger electrons, and secondary electrons) lead to ion desorption (x-ray-induced electron-stimulated desorption) [12], the EICO spectrum exhibits a peak only for the ion desorption initiated by the emission of a selected primary electron. Ionic fragments formed by x-ray-induced electron-stimulated desorption, as well as false counts due to the coincidence of a primary electron emitted from one molecule and an ion dissociated from another molecule, contribute only to a flat background noise. Although reneutralization by electron transfer from the substrate is efficient and far fewer ions than neutrals are desorbed from the surface [13–15], by using the EICO method to detect the surviving ionic fragments we can possibly obtain information about the process initiating the desorption.

Electron-ion coincidence spectroscopy combined with synchrotron radiation has traditionally been developed into a very powerful tool for investigating the

fragmentation dynamics of molecules in the vapor phase [16]. Measurements of energy-selected EICO in the vapor phase, however, are not easy. The coincidence count rate is low even under experimental conditions in which strong irradiation is produced by an undulator beamline, and long data collection times are thus necessary [17]. In contrast, the coincidence count rate is high on a surface because the sample density there is much higher than that in a vapor. Furthermore, in the vapor phase an electric-field gradient applied across a wide ionization region (typically 1 mm) greatly smears the energy distribution of photoelectrons and Auger electrons [18]. An electric-field gradient of 10 V/mm, for example, lowers the energy resolution of the photoelectrons and Auger electrons to more than 10 eV. In contrast, an electric-field gradient applied across the ionization region is low on a surface, and an electric field applied for the purpose of detecting ions does not smear the energy distribution of the photoelectrons and Auger electrons. This makes it easy to use EICO spectroscopy to detect a fragment ion and an energy-selected photoelectron or Auger electron from a surface.

Thus, in 1985 Knotek and Rabalais developed an EICO apparatus combined with an electron beam for surface studies [19]. They applied it to investigate F^+ desorption from a fluorinated, oxidized Ti(100) surface. The coincidence spectra, however, were not clear enough to determine the ion desorption mechanism. Since this pioneering work, however, EICO spectroscopy was not applied for surface studies at all until 1996, because of several problems characteristic to surfaces, such as the abundance of secondary electrons and the high probability of recapture or neutralization of ions.

In 1996, two of the authors (K.M. and M.N.) and their collaborators developed an improved EICO apparatus [20]. It was implemented with an electron beam [20] and synchrotron radiation [21]. Synchrotron radiation is more advantageous than an electron beam because the resonant excitations are accessible and the secondary electrons are drastically reduced. Since then, K.M. and his collaborators have constructed a total of four EICO analyzers [20–26] and are now testing the performance of their latest model [25,26]. EICO spectroscopy has now been widely applied for studies of ion desorption from condensed molecules such as H_2O [23,27–32], NH_3 [33–35], CH_3CN [36–38], $Si(CH_3)_4$ [39], and C_6H_6 [40], and for molecules showing site-specific fragmentation [23,41–45]. This method has also been applied for poly-methylmethacrylate thin film [38,46–48], Si(100) surface terminated by fluorine [22], H_2O dissociatively chemisorbed on a Si(100) surface [H_2O/Si(100)] [31,49,50], $CaF_2(111)$ film epitaxially grown on Si(111) [22,51], and a $TiO_2(110)$ surface [52]. The ion desorption mechanisms that have been elucidated by EICO spectroscopy so far have been described in detail in previous overviews [53–55].

In this article we describe the present status of the EICO apparatus (Sec. 2) and discuss six recent investigations for H_2O (Sec. 3.1.1 and 3.1.2), NH_3 (Sec. 3.2.1 and 3.2.2), CH_3CN (Sec. 3.3), and CF_3CH_3 (site-specific fragmentation, Sec. 3.4) condensed at low temperature. In Sec. 4, we summarize our conclusions and discuss the future direction of EICO spectroscopy in surface science.

2. Electron-ion coincidence apparatus

Figure 1 shows pictures of the first and second EICO analyzers, together with a schematic diagram of the first EICO apparatus implemented with synchrotron radiation. The first analyzer [21] consisted of an electron gun, a coaxial cylindrical mirror analyzer (CMA), a time-of-flight ion mass spectrometer (TOF-MS), a power supply, and an electronic system for measurements. The CMA consisted of a magnetic shield, semi-cylinders 58 and 120 mm in diameter (solid angle = 0.24 sr), three sets of compensation electrodes to maintain a radial electric field, retarding grids, a cylindrical slit, and tandem microchannel plates (MCPs). The CMA had a resolving power of $E/\Delta E = 80$ without a retarding field. The TOF-MS consisted of an electric field shield, a drift tube with an ion-extraction grid ($T1$), a 96-mm drift tube ($T2$ and $T3$), a deflector, a focusing system, and MCPs. The deflector was added to prevent scattered synchrotron radiation and emitted soft x-rays from impinging on the MCPs. The distances between the sample and $T1$, and between $T1$ and $T2$, were 13 and 1 mm, respectively. A pair of conical electrodes was spotwelded to the shield and $T1$ as a lens system to collect ions desorbed into all solid angles. The transmittance of the three meshes inserted perpendicular to the axis of the TOF tube was 0.47, and the ion detection efficiency of the MCPs was 0.60. The angle between the axes of the CMA and the electron gun was 5 deg, and that between the CMA and the TOF-MS was 30 deg. Most of the metallic parts of the CMA were made of SS 316L, whose residual magnetism was diminished by annealing. The CMA, the TOF-MS, and a 75-mm retraction mechanism were mounted on a 203-mm-diameter conflat flange.

The sample surface was excited by synchrotron radiation, and the energy of the emitted electrons was analyzed with the CMA, while the desorbed ions were accelerated towards the TOF-MS. The surface normal

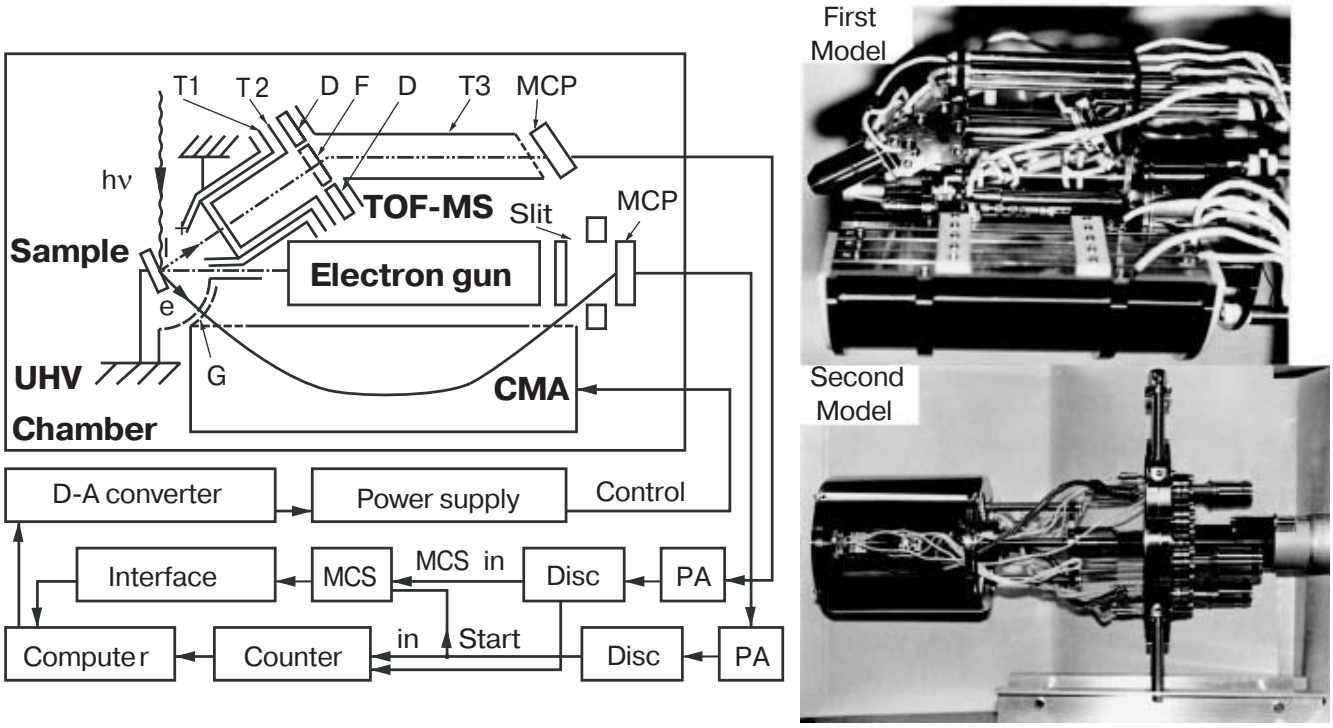

Fig. 1. Pictures of the first and second EICO analyzers and a schematic diagram of the first model implemented with synchrotron radiation. The abbreviations used are defined as follows: PA, preamplifier; Disc, discriminator; T1, drift tube with an extraction grid; T2 and T3, 95-mm drift tube; F, focusing system; D, deflector; G, retarding grids; UHV, ultra high vacuum; MCP, microchannel plate; TOF-MS, time-of-flight ion mass spectrometer; CMA, cylindrical mirror analyzer; MCS, multichannel scaler.

was set coaxial to the TOF-MS. The angle between the surface normal and the synchrotron radiation was 60 deg. The voltage supplies for the CMA were controlled with a personal computer via a D-A converter board. The electron and ion signals were transformed to negative NIM pulses by using preamplifiers and discriminators. The ion counts were recorded, as a function of the TOF difference between the energy-selected electrons and the ions, with a multichannel scaler (MCS) by taking the electron signal as the starting trigger. The MCS was also controlled from the computer via an interface board. Ions desorbed in coincidence with the detected electrons give a coincidence signal at a specific TOF, while ions irrelevant to the electrons increase the background level. As the data accumulation time t_a increases, the ratio of the coincidence signal to the background level improves in proportion to $t_a^{1/2}$, because the background is derived from statistical fluctuations. Since the selected electron kinetic energy corresponds to a particular photoelectron or Auger-electron emission, the coincidence signal intensity represents the yield of the ion desorption induced by the photoelectron emission or Auger process.

The second model [22] did not contain an electron gun and consisted of a CMA, a TOF-MS, and a 50-mm retraction mechanism. The CMA had a solid angle of 1.0 sr (semi-cylinders 56.0 and 132.0 mm in diameter and six sets of compensation electrodes) and a resolving power of $E/\Delta E = 80$. The metallic parts of the analyzer were made of nonmagnetic SS 310.

Figure 2 shows a schematic diagram and picture of the third EICO analyzer [23,24]. To achieve a decent signal-to-background ratio within a reasonable data collection time, the solid angle of the CMA was designed to be 1.1 sr (cylinders 54.0 and 133.0 mm in diameter and six sets of compensation electrodes). The TOF-MS without a deflector was positioned coaxially with the CMA, and the desorbed ions flew straight ahead to the MCPs. With these improvements the signal-to-background ratio was improved by a factor of 5 compared to the second model. The designed resolving power of the CMA was limited to $E/\Delta E = 100$ because of the large solid angle. The actual resolving power, however, was degraded to $E/\Delta E = 80$ due to the ion extraction field (17 V/mm) and the relatively large spot size of the monochromatized synchrotron radiation used (1×1 mm). The resolving power was not im-

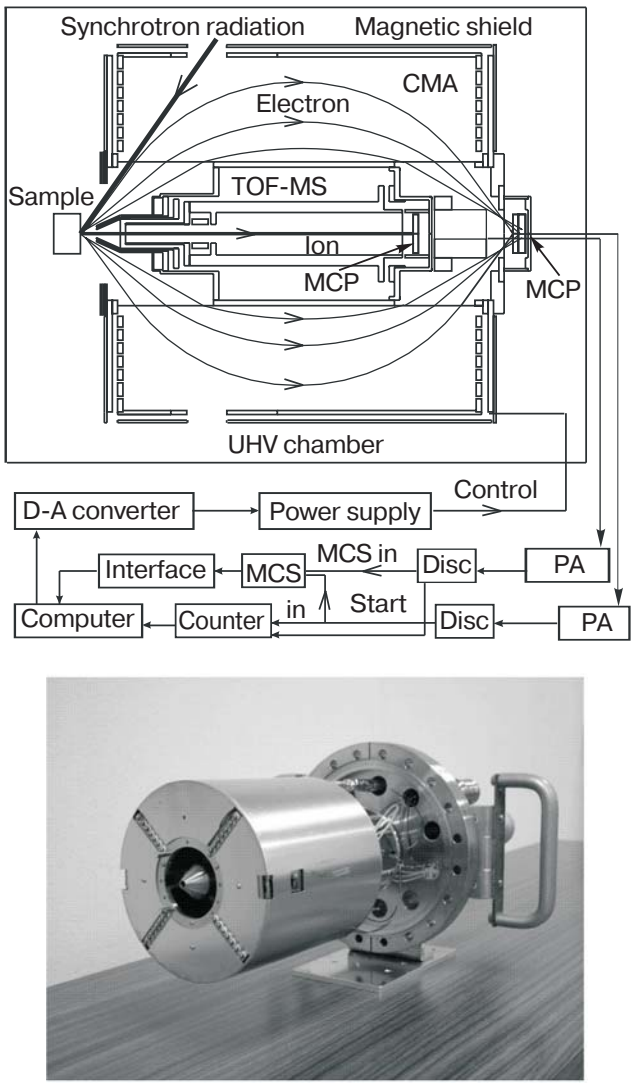

Fig. 2. Schematic diagram and picture of the third EICO analyzer implemented with synchrotron radiation.

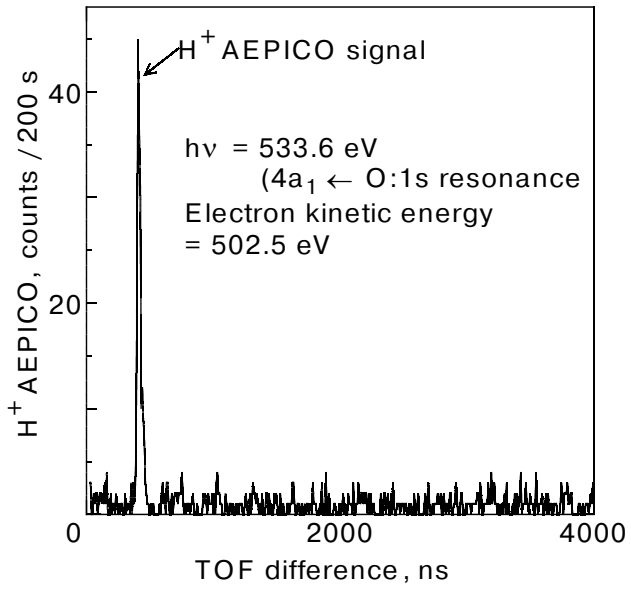

Fig. 3. Typical EICO spectrum of condensed H_2O.

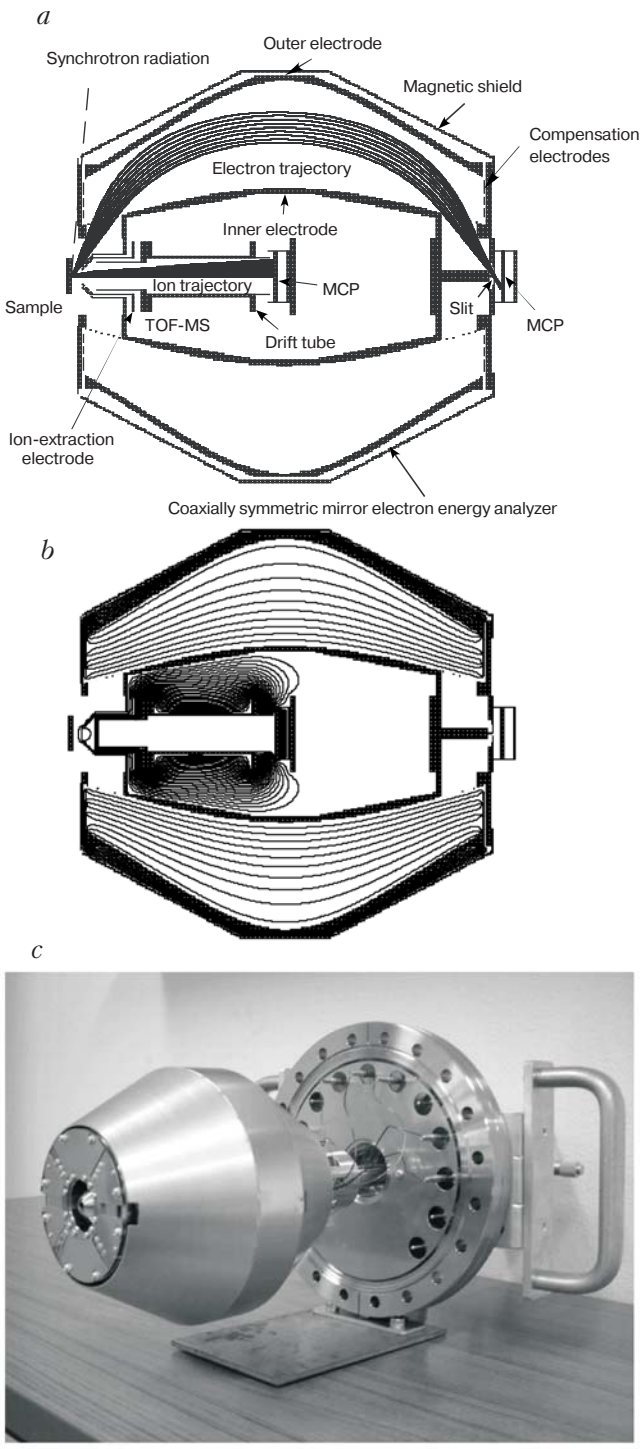

Fig. 4. (*a*) Schematic diagram of the latest EICO analyzer implemented with synchrotron radiation. (*b*) Isoelectric lines simulated with SIMION 3D version 7.0 (Idaho National Engineering and Environmental Laboratory) under the conditions that the voltages of the inner electrode and the magnetic shield are 0 V, that of the outer electrode is −100 V, and that of the ion-extraction grid of the TOF-MS is −30 V. Electron and ion trajectory lines simulated with SIMION 3D are also shown in Fig. 4,*a*, under the conditions that the electron kinetic energy is 182.75 eV and the electron emission angles are 52–67 deg (*c*) Picture of the latest EICO analyzer.

pressive but still effective for various ion desorption studies.

Figure 3 shows a typical EICO spectrum for condensed H_2O (see Sec. 3.1.1) measured with the third EICO analyzer. The influence of the scattered synchrotron radiation and emitted soft x-rays was found to be negligible. The third EICO apparatus is currently active at the BL2B1 beamline installed with a 2-m grasshopper monochromator at the UVSOR synchrotron-radiation facility in Okazaki, Japan. The typical photon intensity is 10^8–10^9 photons/s at an energy resolving power of $E/\Delta E$ = 500. The third EICO apparatus is also used at the BL13 beamline at the HiSOR synchrotron-radiation facility in Higashi-Hiroshima, Japan.

K.M. and his collaborators are now testing the performance of the latest (fourth) model at the PF synchrotron-radiation facility in Tsukuba, Japan (Fig. 4) [25,26]. The advantage of this model is that instead of a conventional CMA, a new coaxially symmetric mirror analyzer developed by Siegbahn et al. [56] is employed as the electron energy analyzer. The analyzer consists of an inner electrode, an outer electrode, three sets of compensation electrodes, and a magnetic shield. The solid angle of this analyzer is designed to be 1.2 sr, while the designed and actual resolving powers are $E/\Delta E$ = 300 and 120, respectively. A short TOF-MS is installed coaxially inside the electron energy analyzer.

The first, second, and third EICO apparatus were used for the investigations described in Sec. 3.2, in Sec. 3.3 and 3.4, and in Sec. 3.1, respectively. Unless otherwise noted, in the investigations described in Sec. 3.1, 3.2.1, and 3.3, the substrate was cooled by liquid nitrogen to about 100 K. In the investigation described in Sec. 3.2.2 and 3.4, the substrate was cooled by flowing cold helium gas to about 50 K. Then, the sample surface was prepared by exposing the substrate to a sample gas or by spraying a sample gas onto the substrate with a pulsed valve.

3. Photo-stimulated ion desorption from condensed molecules studied with EICO spectroscopy

3.1. H_2O

3.1.1. PSID mechanism studied with AEPICO. The most probable model of ion desorption is the Auger-stimulated ion desorption (ASID) mechanism (Fig. 5), which is simply described as a sequence of

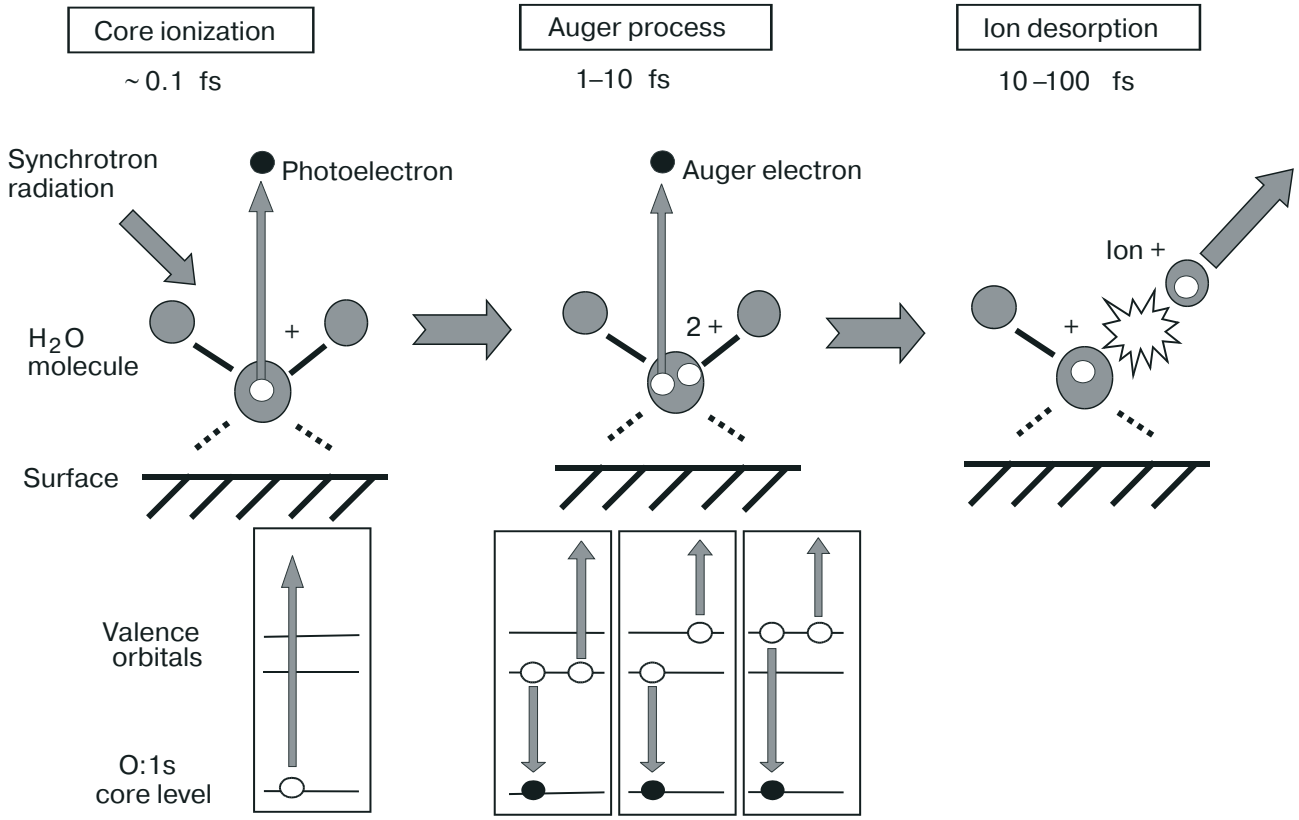

Fig. 5. Three-step H^+ desorption mechanism for the O:1*s* ionization of condensed H_2O (normal ASID): (1) formation of a core-hole by an O:1*s* photoelectron emission (~ 0.1 fs), (2) formation of a two-hole state by an O:KVV transition (1–10 fs), and (3) H^+ desorption induced by Coulomb repulsion between two holes and by electrons missing from O–H bonding orbitals (10–100 fs).

three steps: (1) a core-electron transition leaving a core hole (~ 0.1 fs), (2) an Auger transition leaving multiple valence holes (1–10 fs), and (3) decay of the multi-hole state, causing ion desorption (10–100 fs). The ASID mechanism was initially proposed by Knotek and Feibelman for O^+ desorption induced by Ti:3*p* ionization at a TiO_2 surface, where the driving force was attributed to the Coulomb repulsion between Ti^{2+} and O^+ created by an inter-atomic Auger process [57]. Later, the ASID model was extended for covalently bonded systems [58]. Several theoretical groups reported that two holes are localized on one molecule in Auger final states [59], which are sufficiently long lived to stimulate ion desorption [60–62]. However, the details of the ASID mechanism, the factors that influence desorption probability, and the decay processes competing with desorption have hardly been explored, because there have been no tools for investigating the intermediate Auger transitions responsible for ion desorption. In addition, ion desorption by x-ray-induced electron impact often dominates the primary processes [12]. Recently, however, we have found that Auger electron photoion coincidence (AEPICO) spectroscopy is an ideal tool for investigating the ASID mechanism, because it provides the yield for the ion desorption channel caused by selected Auger transitions.

In this section we describe a study of the H^+ desorption mechanism for the O:1*s* ionization [23,27,29,31,53–55] and resonant excitations [23,28,30,31,54,55] of condensed H_2O by using AEPICO spectroscopy. Since the nature of the surface of condensed H_2O is critically important for many fields, extensive studies have been carried out [63–65]. Ion desorption stimulated by electronic transitions from the O:1*s* core level in condensed H_2O has been investigated theoretically [66], by using an electron beam [67], and by using synchrotron radiation [68,69].

Figure 6 shows the total ion yield (TIY, solid line), Auger electron yield (AEY, dashed line), and TIY/AEY spectra (solid circles) in the range of the O:1*s* excitation of condensed H_2O. The TIY spectrum shows the H^+ desorption yield, as will be described later. The AEY spectrum represents the photoabsorption spectrum in the range of the O:1*s* excitation, and the TIY/AEY intensity is proportional to the number of H^+ ions desorbed per photon absorbed. The TIY/AEY spectrum shows a characteristic threshold peak at the $4a_1 \leftarrow$ O:1*s* resonance ($h\nu$ = 533.6 eV) and a suppression at the $3p \leftarrow$ O:1*s* resonance ($h\nu$ = = 535.4 eV). The spectrum is nearly constant above the O:1*s* ionization threshold ($h\nu$ > 547.6 eV).

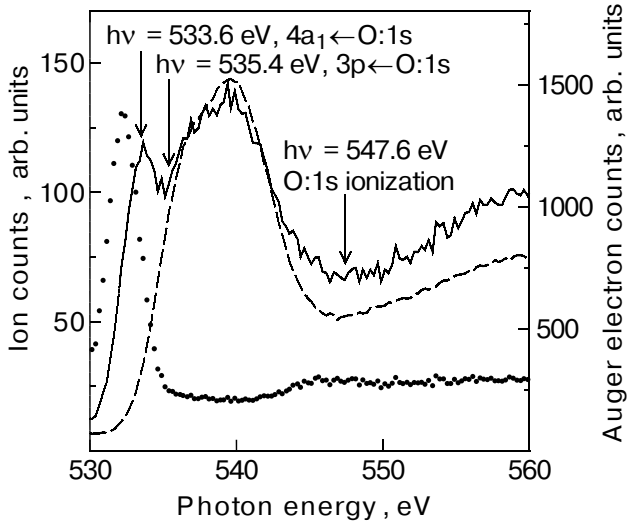

Fig. 6. TIY (solid line), AEY (electron kinetic energy = = 490 eV, dashed line), and TIY/AEY spectra (solid circles) of condensed H_2O. The TIY spectrum shows a $4a_1 \leftarrow$ O:1*s* peak at 533.6 eV, but the peak energy of the TIY/AEY spectrum (532.6 eV) is lower by 1 eV. The reason for this would be that the $4a_1 \leftarrow$ O:1*s* peak energy of surface H_2O, from which ion desorption takes place, is lower than that of bulk H_2O [75] and that excitations by x-ray-induced electrons coming from bulk H_2O induce ion desorption from surface H_2O at 533.6 eV.

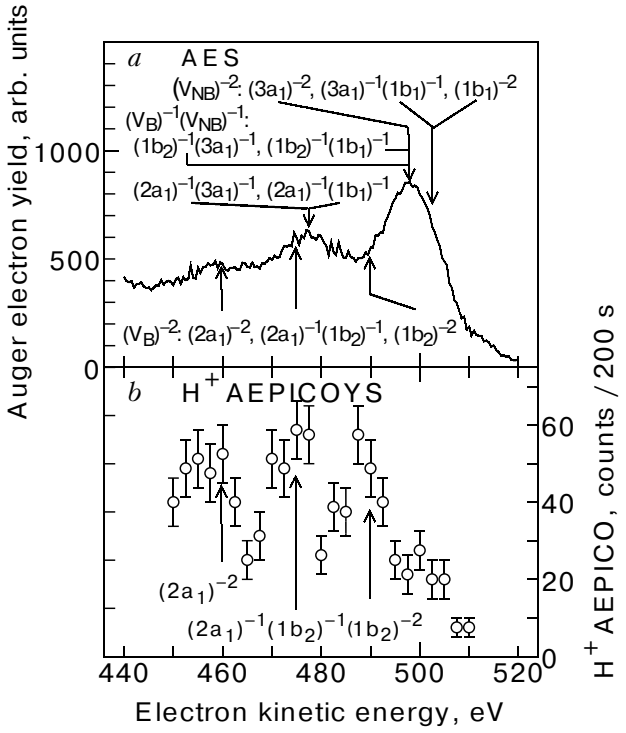

Fig. 7. (*a*) O:1*s* normal AES of condensed H_2O. (*b*) H^+ AEPICOYS for the O:1*s* normal Auger transitions of condensed H_2O. The spectra in panels *a* and *b* were taken at a photon energy of 547.6 eV.

Figure 7,*a* shows the O:1*s* normal Auger-electron spectrum (AES) of condensed H_2O taken at a photon energy of 547.6 eV. The electronic configuration of H_2O is given by $(1a_1)^2(2a_1)^2(1b_2)^2(3a_1)^2(1b_1)^2$, where $1a_1$ is approximately characterized as O:1*s*, $2a_1$ and $1b_2$ as O–H bonding valence orbitals V_B, and $3a_1$ and $1b_1$ as nonbonding lone pair orbitals of oxygen V_{NB} [66]. Accordingly, the Auger final states with two holes are as follows: $(2a_1)^{-2}$, $(2a_1)^{-1}(1b_2)^{-1}$, $(1b_2)^{-2}$, $(2a_1)^{-1}(3a_1)^{-1}$, $(2a_1)^{-1}(1b_1)^{-1}$, $(1b_2)^{-1}(3a_1)^{-1}$, $(1b_2)^{-1}(1b_1)^{-1}$, $(3a_1)^{-2}$, $(3a_1)^{-1}(1b_1)^{-1}$, and $(1b_1)^{-2}$. The peak assignments according to previous reports [70,71] are also shown in Fig. 7,*a*. The O:1*s* Auger intensity is proportional to the Auger transition probability leading to the individual Auger final states with two holes.

Figure 3 shows an example of an AEPICO spectrum of condensed H_2O. One can see that a great portion of the H^+ ions are desorbed coincidentally. Other species such as O^+ and OH^+ are negligible due to the lower desorption efficiencies [69].

Figure 7,*b* shows the H^+ AEPICO-yield spectrum (AEPICOYS), in which the integrated AEPICO count for H^+ is plotted as a function of the Auger-electron kinetic energy. The AEPICO yield is proportional to the product of the Auger transition probability (the formation probability of the Auger final state with two holes) and the ion desorption probability from the Auger final state. By comparing Fig. 7,*a* with Fig. 7,*b*, we can obtain information about the ion desorption probability from the individual Auger final states.

The two–hole states of condensed H_2O are classified into three categories: $(V_B)^{-2}$, $(V_{NB})^{-2}$, and $(V_B)^{-1}(V_{NB})^{-1}$. The order of decreasing Auger electron yield is $(V_{NB})^{-2} > (V_B)^{-1}(V_{NB})^{-1} > (V_B)^{-2}$ (Fig. 7,*a*), while the order of decreasing H^+ AEPICO yield is $(V_B)^{-2} > (V_B)^{-1}(V_{NB})^{-1} > (V_{NB})^{-2}$ (Fig. 7,*b*). Since the number of H^+ ions desorbed per photon absorbed is proportional to the quantity (H^+ AEPICO yield/Auger electron yield), these results show that the order of decreasing number of H^+ ions desorbed per photon absorbed is $(V_B)^{-2} > > (V_B)^{-1}(V_{NB})^{-1} > (V_{NB})^{-2}$. As the number of holes in V_B increases, the number of H^+ ions desorbed per photon absorbed increases. Thus, the normal ASID mechanism is reasonable and the cause of the H^+ desorption is the Coulomb repulsion between the two holes formed in V_B (Fig. 5). As H^+ ions are released into the vacuum due to the Coulomb repulsion between H^+ and OH^+, the OH^+ ions are pushed toward the substrate and neutralized or recaptured.

Next we describe a study of the H^+ desorption mechanism for the $4a_1 \leftarrow$ O:1*s* resonant excitation of condensed H_2O [23,28,30,31,54,55]. As shown in Fig. 6, the H^+ desorption yield has a characteristic threshold peak at the $4a_1 \leftarrow$ O:1*s* resonance. The H^+ desorption mechanism for the $4a_1 \leftarrow$ O:1*s* resonance thus seems very different from that in the O:1*s* ionization. The subject of the H^+ desorption mechanism for the $4a_1 \leftarrow$ O:1*s* resonant excitation is interesting from the viewpoint of ultra-fast photodissociation; that is, bond breaking during the lifetime of the core-excited state. Ultra-fast photodissociation was, for the first time, found in the $4p\sigma^* \leftarrow$ Br:3*d* resonance of HBr [72]. Evidence for the ultra-fast photodissociation of neutral H has also been shown for the $4a_1 \leftarrow$ O:1*s* resonance of isolated H_2O [73,74]. The neutral H yields from condensed H_2O and condensed NH_3, however, show no enhancement by ultra-fast dissociation in the $4a_1 \leftarrow 1s$ resonance [75].

Figure 8,*a* shows the $4a_1 \leftarrow$ O:1*s* resonant AES of condensed H_2O taken at a photon energy of 533.6 eV (solid line), together with the normal AES taken at a photon energy of 547.6 eV (dashed line). The spectator Auger transition, in which the excited electron does not participate, occurs primarily in the resonant Auger transition [74]. When the resonant tunneling of the excited electron to a neighboring molecule accelerates the delocalization of the electron, the normal Auger transition is seen, in addition to the spectator Auger transition, in the AES [76–78]. Thus, for the solid

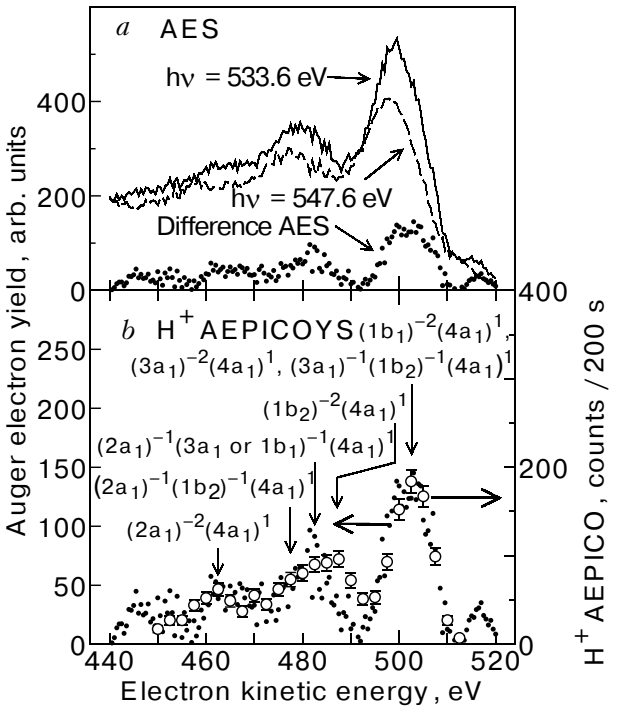

Fig. 8. (*a*) $4a_1 \leftarrow$ O:1*s* spectator AES (solid line), O:1*s* normal AES (dashed line), and Difference AES (solid circles) of condensed H_2O; (*b*) H^+ AEPICOYS for the $4a_1 \leftarrow$ O:1*s* spectator Auger transitions (open circles) and Difference AES (solid circles) of condensed H_2O.

line in Fig. 8,*a*, the normal AES is likely to be superimposed on the spectator AES. In the AES the peak of the spectator Auger transition is located a few electron volts above that of the corresponding normal Auger transition, because the excited electron shields the hole-hole Coulomb repulsion and stabilizes the spectator Auger final state. To obtain the pure spectator AES, we subtracted the dashed line from the solid line in Fig. 8,*a* (Difference AES). The pure spectator AES thus obtained (solid circles in Figs. 8,*a* and *b*) shows three peaks at 502.5, 482.5, and 462.5 eV. Since the peak of the spectator Auger transition is, as described above, located a few electron volts above that of the normal Auger transition (Fig. 7,*a*), these three peaks at 502.5, 482.5, and 462.5 eV are assigned to the spectator Auger final states with characters of $(O{:}2p)^{-2}(4a_1)^1$, $(2a_1)^{-1}(O{:}2p)^{-1}(4a_1)^1$, and $(2a_1)^{-2}(4a_1)^1$, respectively [70,71]. Here, O:2*p* denotes a $1b_2$, $3a_1$, or $1b_1$ orbital.

Figure 8,*b* shows the H^+ AEPICOYS for the $4a_1 \leftarrow$ O:1*s* spectator Auger transitions (open circles), together with the Difference AES (solid circles, the same data as in Fig. 8,*a*). Since the three peaks of the H^+ AEPICOYS are at the same positions as the peaks of the Difference AES and the two spectra are similar to each other, the H^+ desorption is considered to be caused by the spectator Auger transition. The spectator Auger intensity is proportional to the Auger transition probability leading to the individual Auger final states with two holes in some valence orbitals and an excited electron in the $4a_1$ orbital. The H^+ AEPICOYS intensity is proportional to the product of the spectator Auger transition probability and the H^+ desorption probability from the Auger final state. Therefore, the H^+ desorption probability seems to be independent of the valence orbitals occupied by holes in the spectator Auger final state.

In addition to these results, we must take two facts into account to understand the H^+ desorption mechanism for the $4a_1 \leftarrow$ O:1*s* resonance. One is that the potential surface of the $(O{:}1s)^{-1}(4a_1)^1$ state is repulsive with respect to the O–H direction, because the $4a_1$ orbital is an antibonding orbital of the O–H bond. The other is that the period of the O–H stretching vibration is comparable to the lifetime of the O:1*s* hole. On the basis of the experimental results and these two facts, we propose a four-step H^+ desorption mechanism for the $4a_1 \leftarrow$ O:1*s* resonance (Fig. 9): (1) the $4a_1 \leftarrow$ O:1*s* transition, (2) extension of the HO–H distance in the $(O{:}1s)^{-1}(4a_1)^1$ state (ultra-fast OH extension), (3) a spectator Auger transition leading to a two–hole state with an excited electron in the $4a_1$ orbital, and (4) H^+ desorption taking place in turn. The increase in the TIY/AES spectrum at the $4a_1 \leftarrow$ O:1*s* resonance (Fig. 6) is driven mainly by the O–H repulsive potential surface of the $(O{:}1s)^{-1}(4a_1)^1$ state.

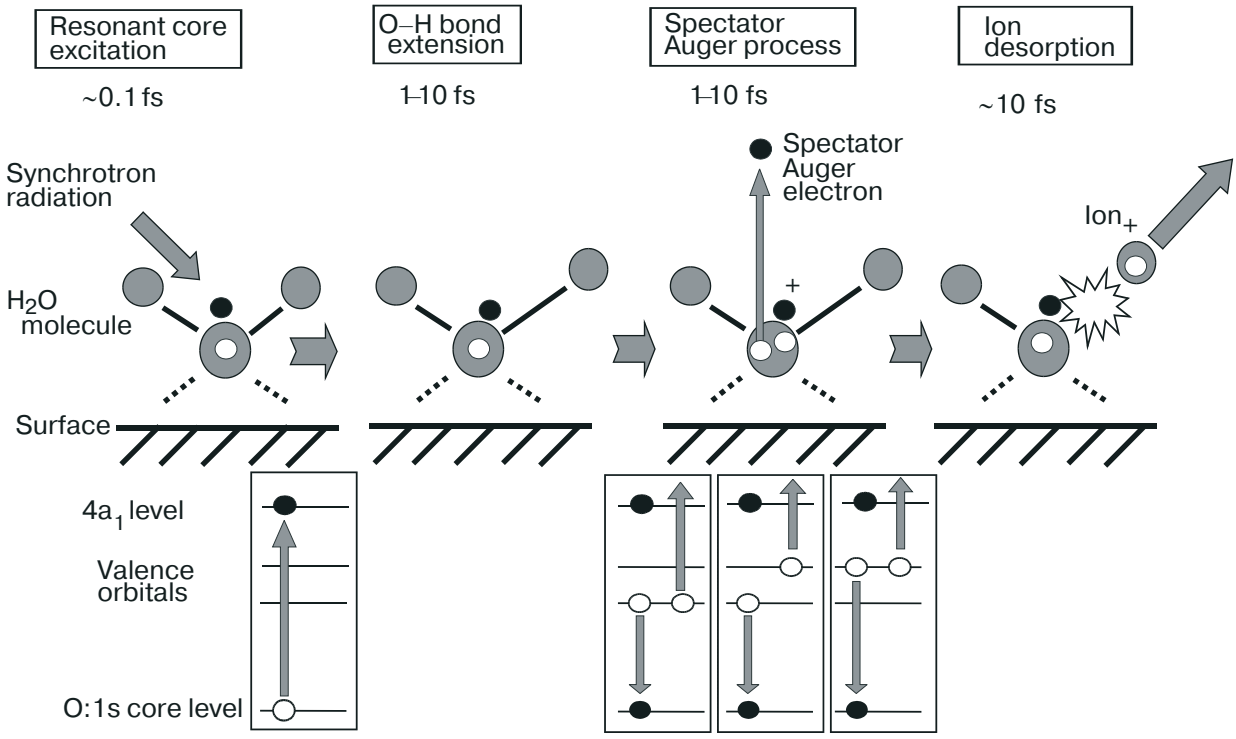

Fig. 9. Four-step H^+ desorption mechanism for the $4a_1 \leftarrow$ O:1*s* resonance of condensed H_2O: (1) the $4a_1 \leftarrow$ O:1*s* transition, (2) extension of the HO–H distance in the $(O{:}1s)^{-1}(4a_1)^1$ state, (3) a spectator Auger transition leading to a two-hole state with an excited electron in the $4a_1$ orbital, and (4) H^+ desorption. The H^+ desorption is driven mainly by the O–H repulsive potential surface of the $(O{:}1s)^{-1}(4a_1)^1$ state.

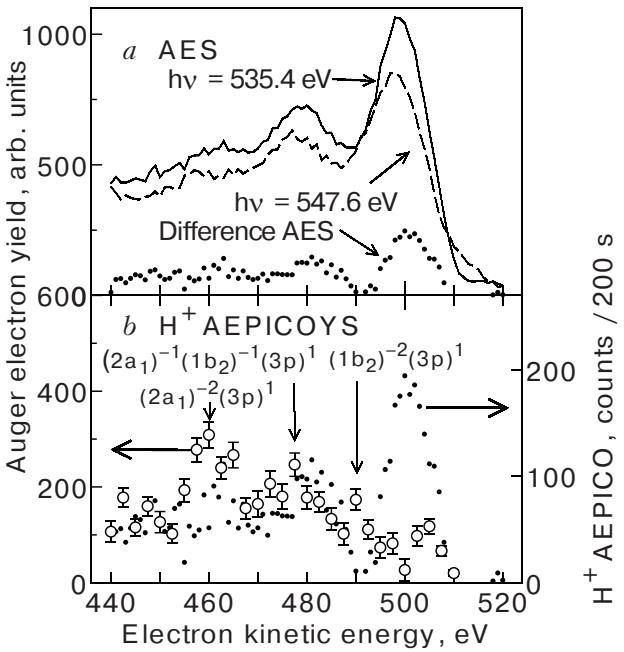

Fig. 10. (*a*) $3p \leftarrow$ O:1*s* spectator AES (solid line), O:1*s* normal AES (dashed line), and Difference AES (solid circles) of condensed H_2O. (*b*) H^+ AEPICOYS for the $3p \leftarrow$ O:1*s* spectator Auger transitions (open circles) and Difference AES (solid circles) of condensed H_2O.

Next we describe a study of the H^+ desorption mechanism for the $3p \leftarrow$ O:1*s* resonant excitation of condensed H_2O [23,30,31,54]. Figure 10,*a* shows the $3p \leftarrow$ O:1*s* spectator AES of condensed H_2O taken at a photon energy of 535.4 eV (solid line), together with the normal AES taken at a photon energy of 547.6 eV (dashed line). Figure 10,*b* shows the H^+ AEPICOYS in the $3p \leftarrow$ O:1*s* spectator Auger transitions (open circles). At the 3*p* resonance ($h\nu$ = 535.4 eV), the AEPICOYS displays major, medium, and minor peaks at electron kinetic energies of 460, 475, and 490 eV, respectively. According to previous reports [70,71], these peaks are assigned to the $(2a_1)^{-2}(3p)^1$, $(2a_1)^{-1}(1b_2)^{-1}(3p)^1$, and $(1b_2)^{-2}(3p)^1$ spectator Auger final states. The Difference AES obtained by subtracting the AES at the O:1*s* ionization ($h\nu$ = = 547.6 eV) from that at the $3p \leftarrow$ O:1*s* resonance ($h\nu$ = 535.4 eV) is also shown in Fig. 10 (solid circles). The Difference AES is expected to correspond to the pure spectator Auger component, as described above. The remarkable difference in spectral shape between the Difference AES and the AEPICOYS shows that the H^+ desorption probability varies with the spectator Auger final state. In contrast to the $4a_1 \leftarrow$ O:1*s* spectator Auger transition, the H^+ desorption probability depends on the valence orbitals occupied by holes in the $3p \leftarrow$ O:1*s* spectator Auger final state. This result indicates that the pure spectator ASID mechanism is responsible for the $3p \leftarrow$ O:1*s* resonance; that is, the repulsive potential surface of the (valence orbitals)$^{-2}(3p)^1$ state is responsible for the H^+ desorption.

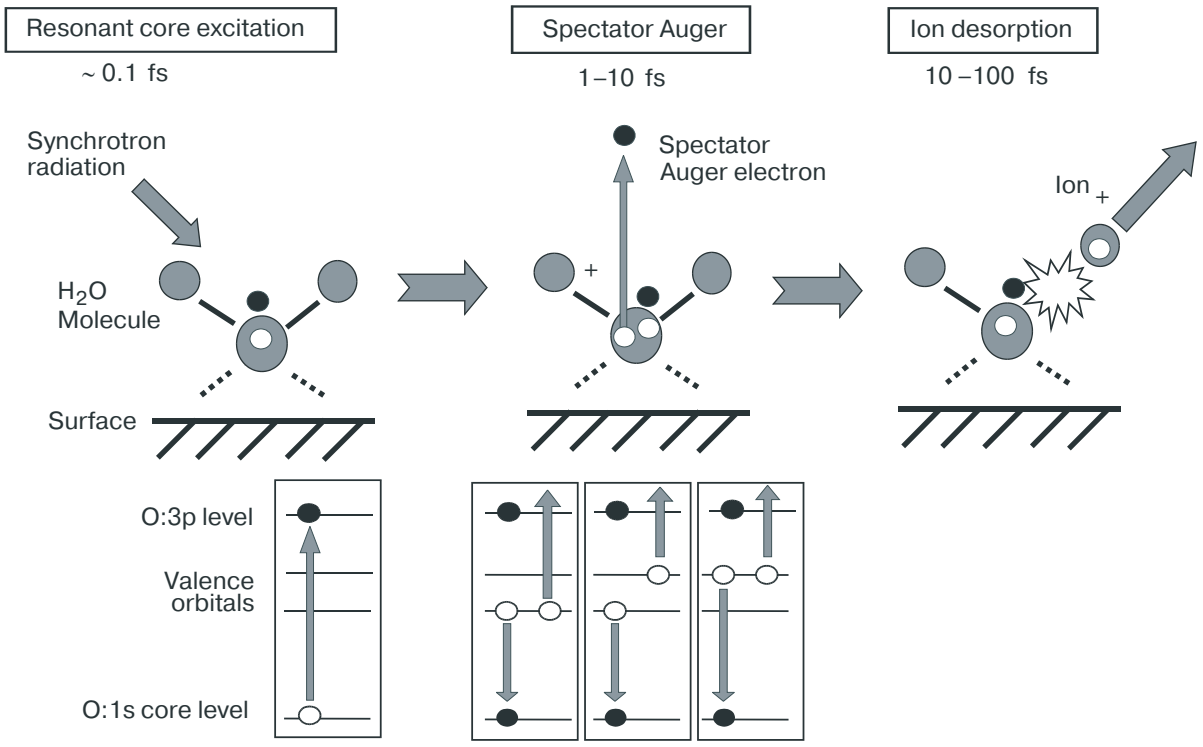

Fig. 11. Three-step H^+ desorption mechanism for the $3p \leftarrow$ O:1*s* resonance of condensed H_2O: (1) the $3p \leftarrow$ O:1*s* transition, (2) a spectator Auger transition, and (3) H^+ desorption. The H^+ desorption is suppressed by the reduction in the hole-hole Coulomb repulsion due to shielding by the 3*p* electron.

On the basis of these results, we propose a three-step H^+ desorption mechanism for the $3p \leftarrow$ O:1*s* resonance (Fig. 11): (1) the $3p \leftarrow$ O:1*s* transition, (2) a spectator Auger transition, and (3) H^+ desorption taking place in turn. In contrast to the $4a_1 \leftarrow$ O:1*s* resonance, the HO–H distance is not extended before the Auger process. This is because the potential surface of the $(O:1s)^{-1}(3p)^1$ state is expected to be similar to that of the ground state, because the O:1*s* and 3*p* orbitals are irrelevant to the O–H bonding. The decrease in the TIY/AES spectrum at the $3p \leftarrow$ O:1*s* resonance (Fig. 6) is attributed to the reduction in the hole-hole Coulomb repulsion due to shielding by the 3*p* electron.

3.1.2. Determination of O:*1s level of* H_2O *from which* H^+ *is desorbed in PSID of condensed* H_2O. Core-level photoelectron spectroscopy, also called x-ray photoelectron spectroscopy (XPS), has been used to investigate solids and their surfaces [79]. This technique is surface sensitive due to the small escape depth of photoelectrons. As described in Sec. 3.1.1, by using EICO spectroscopy it is possible to obtain the kinetic energy spectrum of the electron that coincides with a specific ion desorption (for example, see Figs. 7,*b*, 8,*b*, and 10,*b*). Therefore, because ions have an even shorter escape depth than electrons, EICO spectroscopy can be used as an extremely surface-sensitive form of XPS [80]. That is, although conventional XPS detects core-level photoelectron emission from the bulk of a solid (within the escape depth of the photoelectron), EICO spectroscopy selectively detects photoelectron emissions from the upper molecular layers (especially the uppermost molecular layer) of a surface. As a result, the so-called surface core-level shift can easily be observed. In this section, we apply the EICO technique to a surface of condensed H_2O to detect the surface core-level shift of the O:1*s* level [23,32], thus demonstrating the advantages and possibilities of EICO spectroscopy for surface analysis.

Since the nature of the surface of condensed H_2O is of critical importance in many fields (as mentioned in Sec. 3.1.1), this topic has been studied extensively [63–65]. According to one previous study [63], the surface of condensed H_2O contains several types of H_2O molecules, including two- or three-coordinated molecules with a dangling hydrogen, two- or three-coordinated molecules with a dangling oxygen coordination, and four-coordinated molecules with distorted tetrahedron. Although condensed H_2O has been studied by XPS [81,82], to the best of our knowledge no study has examined the surface core-level shift of the O:1*s* level at the surface of condensed H_2O.

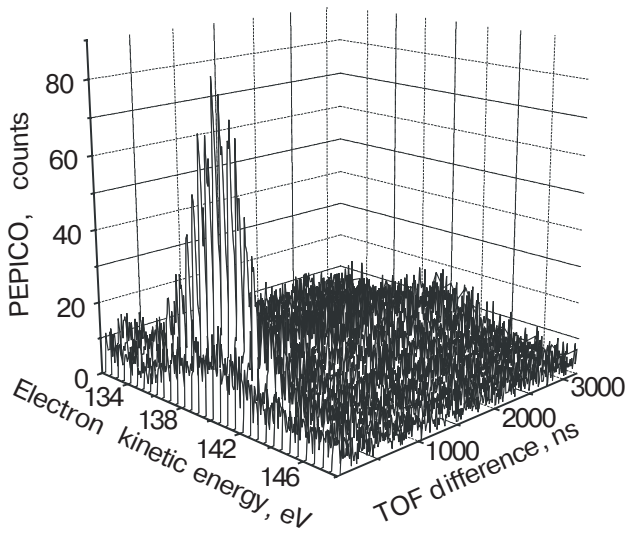

Fig. 12. A series of PEPICO spectra for H_2O condensed on a TiO_2(110) surface. These spectra were taken, at intervals of 0.5 eV in electron kinetic energy, at a photon energy of 680 eV.

Figure 12 shows a series of O:1*s* photoelectron-photoion coincidence (PEPICO) spectra for H_2O condensed on a TiO_2(110) surface. These spectra were taken, at intervals of 0.5 eV in electron kinetic energy, at a photon energy of 680 eV. The H^+ desorption intensity reaches its maximum around an electron kinetic energy of 139 eV.

Figure 13 shows the H^+ PEPICO-yield spectrum (PEPICOYS, solid squares), in which the integrated PEPICO count for H^+ in Fig. 12 is plotted as a function of the electron kinetic energy. The figure also shows the photoelectron spectrum (PES) obtained under the same conditions (open circles). The Gaussian curves drawn with linear backgrounds (solid lines) were calculated by the least-squares fitting method. The small peak at 144 eV in the PES is due to O:1*s* photoelectron emission from the substrate. The peak of the H^+ PEPICOYS is not located at the same energy as the peak of the PES, but rather is shifted to a lower kinetic energy by about 0.7 eV.

The reason for the peak shift between the H^+ PEPICOYS and the PES is that the O:1*s* binding energy of H_2O from which H^+ is desorbed in PSID is different from the O:1*s* binding energies of the other types of H_2O molecules. In the upper molecular layers at the surface of condensed H_2O, some of the hydrogen bonds between molecules are broken, forming dangling hydrogens. It seems reasonable to assume that the H^+ ions are desorbed from the molecules with the dangling hydrogens (probably two-coordinated molecules), because these hydrogens are easily

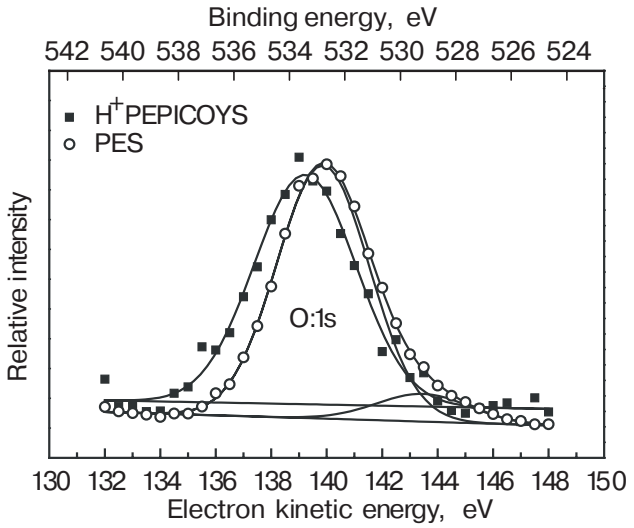

Fig. 13. H^+ PEPICOYS (solid squares) and PES (open circles) for H_2O condensed on a TiO_2(110) surface ($h\nu$ = = 680 eV). The Gaussian curves drawn with linear backgrounds (solid lines) were calculated by the least-squares fitting method.

desorbed. Thus, the PEPICOYS only reflects the binding energy of an oxygen atom bonded to a dangling hydrogen atom in (or located very close to) the uppermost molecular layer. Meanwhile, since the O:1*s* photoelectron is emitted from all the oxygen atoms within the escape depth of the photoelectron, the observed peak in the PES is a convolution of many peaks for the photoelectrons emitted from all the bulk species located within the escape depth.

Previously, it was reported that the O:1*s* binding energy observed in the XPS spectrum of bulk H_2O was shifted by −7.1 eV [81] (without a correction in the work function) or −2.3 eV [82] (with a correction in the work function) from that of H_2O vapor. The O:1*s* binding energy of the less coordinated molecules, which contain dangling hydrogens in (or very close to) the uppermost molecular layer, is expected to fall within the range between that of the bulk and that of the vapor phase, because the properties of the less coordinated molecules are expected to be somewhere between those of fully coordinated molecules in bulk H_2O and those of H_2O molecules in the vapor phase. In fact, this assumption is consistent with the result that the binding energy of the less coordinated H_2O molecules is shifted by +0.7 eV from that of bulk H_2O (Fig. 13). The peaks caused by the less coordinated H_2O molecules are negligible in the PES (Fig. 13) because those H_2O molecules are a very small fraction of the bulk H_2O [63].

Our view is supported by comparing the results for $H_2O/Si(100)$ and H_2O condensed on Si(100) at 100 K under the same experimental conditions. It is known that H_2O is dissociatively chemisorbed to form Si–OH and Si–H species on the Si(100) surface at room temperature [64]. The H^+ PEPICOYS and PES exhibit peaks at similar electron kinetic energies in $H_2O/Si(100)$ because all the oxygen atoms at the Si(100) surface are present as an OH species. There is no reason to expect a peak shift between the H^+ PEPICOYS and the O:1*s* PES for $H_2O/Si(100)$ because each method depends on the same OH species, in contrast to the case of condensed H_2O. However, for H_2O condensed on Si(100), the 0.7-eV shift shown in Fig. 13 was also observed, in contrast to the case of $H_2O/Si(100)$.

To the best of our knowledge, this is the first observation of the surface core-level shift of condensed H_2O. This demonstrates the advantages and possibilities of EICO spectroscopy for surface analysis. EICO spectroscopy can thus be used as a form of extremely surface-sensitive and site-specific XPS. Moreover, EICO spectroscopy can be used to investigate the chemical conditions of surfaces, because ion desorption is strongly affected by the surface chemical bonds and the relaxation process of the excited state.

3.2. NH_3

3.2.1. PSID mechanism studied with AEPICO. In this section we describe a study using EICO spectroscopy to examine the H^+ desorption mechanism for the N:1*s* ionization [33,53] and the resonant excitation [34] of condensed NH_3. Figure 14 shows a series of AEPICO spectra for the N:KVV normal Auger transi-

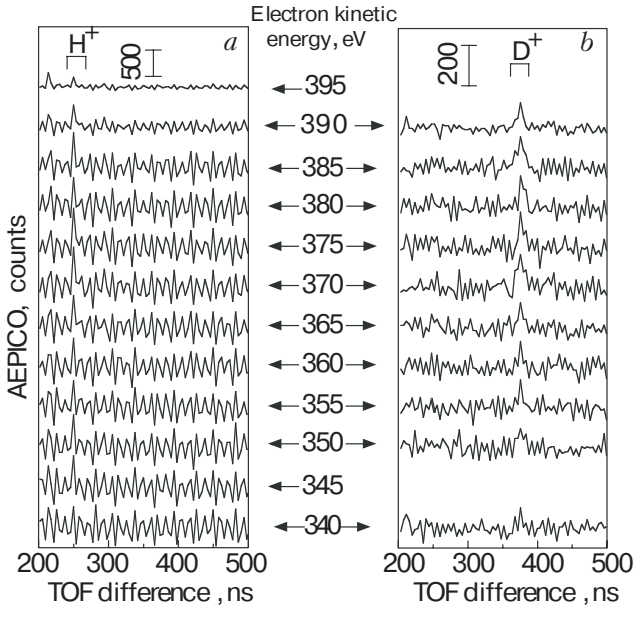

Fig. 14. AEPICO spectra for the N:KVV normal Auger transitions of condensed NH_3 (*a*) and condensed ND_3 (*b*). The spectra were taken at a photon energy of 429 eV.

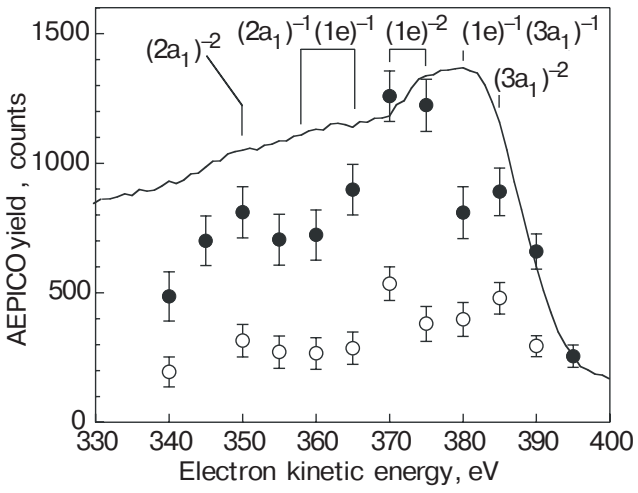

Fig. 15. AEPICOYS for H^+ (solid circles) and D^+ (open circles), and AES (solid line) for the N:KVV normal Auger transitions of condensed NH_3 (ND_3). The spectra were taken at a photon energy of 429 eV.

tions of condensed NH_3 (*a*) and ND_3 (*b*). A peak located in a TOF difference range of 246–258 ns for NH_3 (Fig. 14,*a*) is assigned to the true coincidence signal of H^+, while a peak between 366–382 ns for ND_3 (Fig. 14,*b*) is assigned to D^+. The normal AEPICO spectra of condensed NH_3 and ND_3 exhibit only H^+ and D^+, respectively.

Figure 15 shows the normal AEPICOYS for H^+ and D^+ in condensed NH_3 (solid circles) and ND_3 (open circles), together with the AES (solid line). The AEPICO yields of both H^+ and D^+ are enhanced at the electron kinetic energy of the N:KVV Auger transition. These results show that the photoions are produced through normal ASID, in which the N:KVV Auger decay stimulates cleavage of an N–H or N–D bond (Fig. 5). The fine structures of these AEPICOYS, however, are different from those of the AES. Accordingly, we conclude that the probability of normal ASID depends on the Auger final state, as in condensed H_2O (Fig. 7).

The electronic configuration of NH_3 is $(1a_1)^2(2a_1)^2(1e)^4(3a_1)^2$. The $1a_1$ is characterized as the core level (N:1*s*), the $2a_1$ and $1e$ orbitals are classified as bonding orbitals V_B, and the $3a_1$ orbital with the character of a nitrogen lone pair is classified as a weak bonding orbital V_{WB} because it is spread out somewhat toward the N–H bond. Based on a previous report by Larkins and Lubenfeld [83], the energy positions of the Auger final states are given in Fig. 15. The Auger final states with characters of $(2a_1)^{-2}$, $(2a_1)^{-1}(1e)^{-1}$, and $(1e)^{-2}$ correspond to the normal Auger process of KV_BV_B, while those for $(2a_1)^{-1}(3a_1)^{-1}$ and $(1e)^{-1}(3a_1)^{-1}$ correspond to KV_BV_{WB}, and that of $(3a_1)^{-2}$, to $KV_{WB}V_{WB}$.

The AEPICO yields of H^+ and D^+ are enhanced at the electron kinetic energy associated with $(1e)^{-2}$, while the Auger electron yield is significantly enhanced in the $(1e)^{-1}(3a_1)^{-1}$ and $(3a_1)^{-2}$ Auger final states. As in the case of condensed H_2O, these results indicate that KV_BV_B leads to normal ASID more efficiently than $KV_{WB}V_B$ or $KV_{WB}V_{WB}$.

The AEPICO yield of D^+ is one-third to one-half that of H^+ over the whole electron kinetic energy range studied (Fig. 15). This result indicates that H^+ has a high yield (because of its low mass and fast exit velocity), reducing the effectiveness of reneutralization relative to D^+ [84–86].

We also studied the H^+ desorption at the $4a_1 \leftarrow$ N:1*s* resonant excitation of condensed NH_3 [34]. The TIY/AEY spectrum showed a characteristic threshold peak at the $4a_1 \leftarrow$ N:1*s* resonance. The peak position of the H^+ AEPICOYS was found to be the same as that of the resonant AES. These results suggest that H^+ is desorbed by a four-step mechanism similar to that of condensed H_2O at the $4a_1 \leftarrow$ O:1*s* resonance; that is, the mechanism consists of (1) the $4a_1 \leftarrow$ N:1*s* transition, (2) extension of the H_2N–H distance in the $(N{:}1s)^{-1}(4a_1)^1$ state, (3) a spectator Auger transition leaving the $(\text{valence})^{-2}(4a_1)^1$ state, and (4) H^+ desorption. This was difficult to conclude, however, because the electrons emitted from bulk NH_3 dominated those emitted from the upper molecular layers from which H^+ could be desorbed.

3.2.2. Sub-monolayer adsorbed on Xe *film.* As suggested in Sec. 3.2.1, to clarify the H^+ desorption mechanism for the $4a_1 \leftarrow$ N:1*s* resonant excitation of NH_3, it is necessary to investigate an NH_3 sub-monolayer adsorbed on a chemically inactive sub-

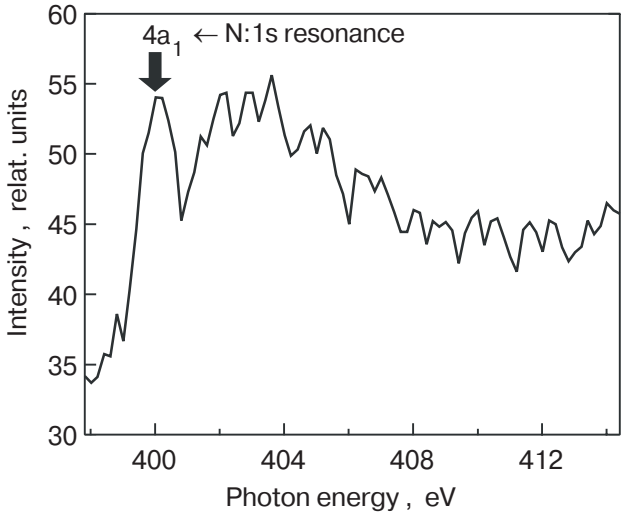

Fig. 16. TIY of NH_3/Xe, which shows the H^+ desorption yield.

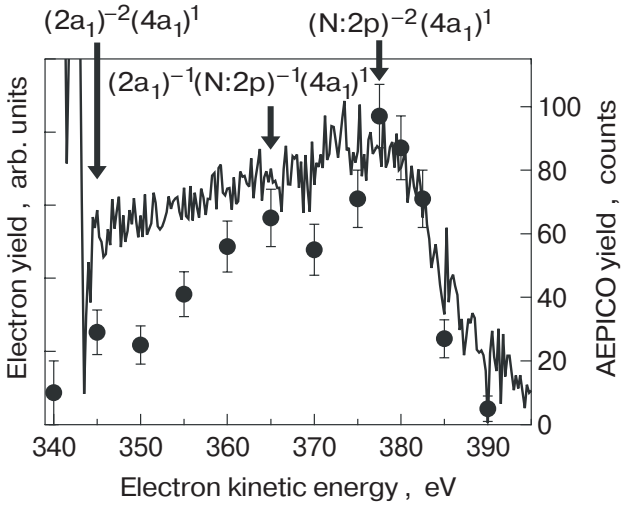

Fig. 17. H^+ AEPICOYS for the $4a_1 \leftarrow$ N:1*s* spectator Auger transitions ($h\nu$ = 400 eV, solid circles) and Difference AES (solid line, pure spectator AES) of NH_3/Xe.

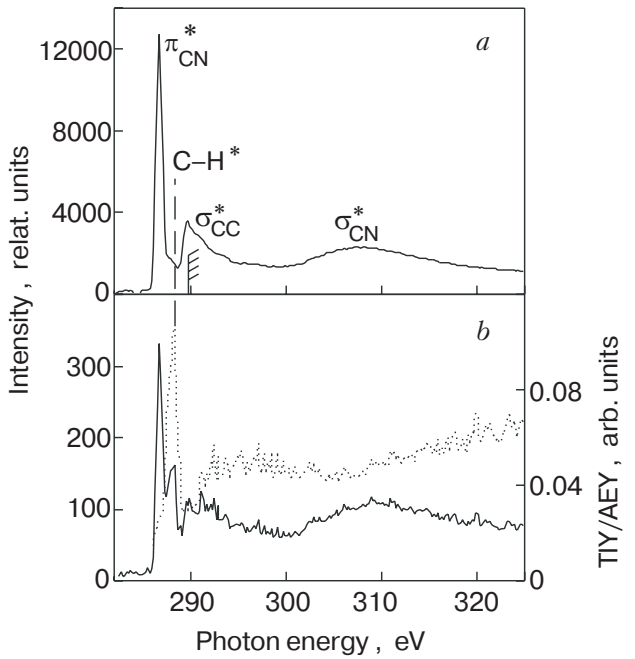

Fig. 18. AEY (*a*, solid line, electron kinetic energy = 255 eV), TIY (*b*, solid line), and TIY/AEY (*b*, dashed line) in the range of the C:1*s* excitation of condensed CH_3CN. The hatching in (*a*) shows the ionization limit taken from Ref. 90.

stance. Accordingly, we studied the H^+ desorption of an isolated NH_3 sub-monolayer adsorbed on a Xe film (NH_3/Xe) [35]. The NH_3/Xe sample was prepared by exposing a gold foil to 300 L (1 L = $1\cdot10^{-6}$ Torr·s) of Xe followed by exposure to 1 L of NH_3, and the coverage of NH_3 is less than 1 ML (unity sticking factor, monolayers). Figure 16 shows the TIY spectrum in the range of the N:1*s* excitation of NH_3/Xe. This spectrum is similar to that reported for condensed NH_3 by Menzel et al. [87] and displays a characteristic threshold peak at a photon energy of 400 eV. The peak is assigned to the resonant excitation from N:1*s* to the $4a_1$ orbital with an N–H antibonding character [88].

Figure 17 shows the H^+ AEPICOYS for the $4a_1 \leftarrow$ N:1*s* spectator Auger transitions (solid circles), together with the Difference AES (solid line, pure spectator AES). Three peaks in the AEPICOYS are assigned to the spectator Auger final states with characters of $(2a_1)^{-2}(4a_1)^1$, $(2a_1)^{-1}(N:2p)^{-1}(4a_1)^1$, and $(N:2p)^{-2}(4a_1)^1$. Here, N:2*p* denotes the 1*e* or $3a_1$ orbital. Since the shape of the AEPICOYS roughly looks like that of the spectator AES, the four-step H^+ desorption mechanism (Fig. 9) is the most plausible mechanism for the $4a_1 \leftarrow$ N:1*s* resonance of NH_3, as in the $4a_1 \leftarrow$ O:1*s* resonance of condensed H_2O.

3.3. CH_3CN

In this section we describe a study using EICO spectroscopy to investigate the H^+ desorption mechanism for the C:1*s* resonant excitation [36–38] of condensed CH_3CN (acetonitrile). The valence electronic configuration of CH_3CN is $(6a_1)^2(1e)^4(7a_1)^2(2e)^4$ [89]. The characters of the $6a_1$, 1*e*, $7a_1$, and 2*e* orbitals are the $\sigma_{C\text{-}C}$ (including the C:2*s* character), π_{CH3} (pseudo π), σ_{CN}, and π_{CN} bonding orbitals, respectively.

Figure 18 shows the AEY (*a*, solid line), TIY (*b*, solid line), and TIY/AEY spectra (*b*, dashed line) in the range of the C:1*s* excitation of condensed CH_3CN. The AEY spectrum is close to the carbon-K near-edge spectrum of condensed CH_3CN reported by Stevens et al. [90]. The most intense peak corresponds to the $\pi^*_{CN} \leftarrow$ C:1*s* resonance. The assignments of the structures in the AEY spectrum are shown in Fig. 18,*a*. The TIY spectrum in Fig. 18,*b* shows the H^+ desorption yield, as will be described later. The TIY/AEY spectrum shows a large peak at the C–H* $\leftarrow$ C:1*s* resonance (288.1 eV, Fig. 18,*b*). This fact indicates that the desorption efficiency increases substantially at the C–H* $\leftarrow$ C:1*s* resonance.

We made AEPICO measurements at the $\pi^*_{CN} \leftarrow$ C:1*s*, C–H* $\leftarrow$ C:1*s*, $\sigma^*_{CC} \leftarrow$ C:1*s*, and $\sigma^*_{CN} \leftarrow$ C:1*s* resonances of condensed CH_3CN. Figure 19 shows a series of spectator AEPICO spectra taken at the C–H* $\leftarrow$ C:1*s* resonance ($h\nu$ = 288.1 eV). The dominant peak at 528 ns was assigned to the H^+ signal. Ionic species other than H^+ were negligible in the AEPICO spectra. We also made AEPICO measurements at other photon energies in the C:KVV Auger-electron transition, but ions other than H^+ were also negligible in this case. We consider the reneutralization of

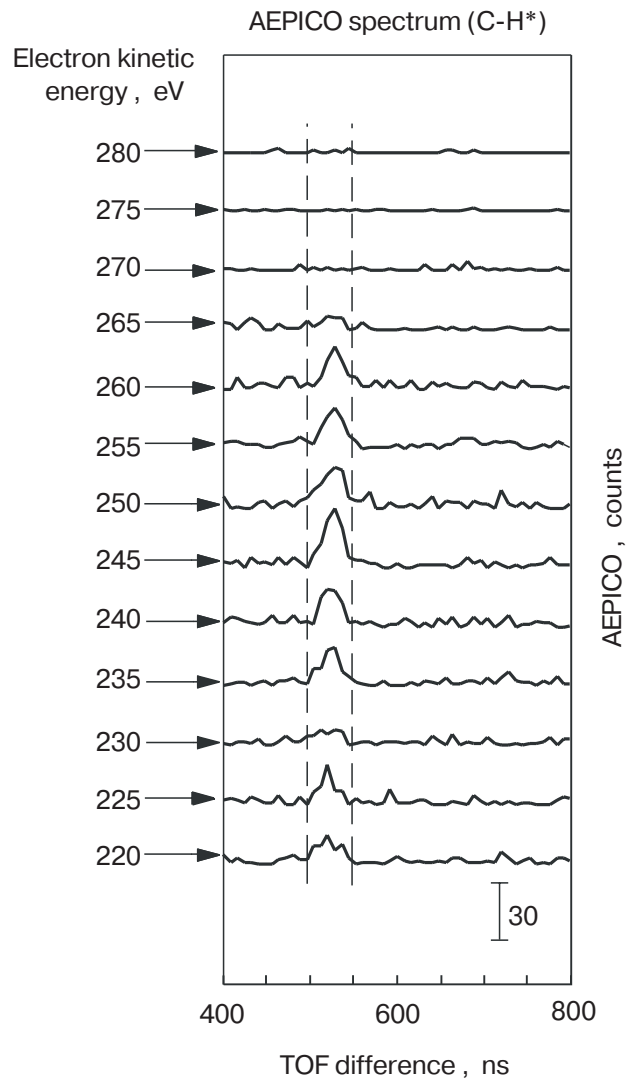

Fig. 19. A series of spectator AEPICO spectra taken at the C–H* ← C:1*s* resonance ($h\nu$ = 288.1 eV) of condensed CH_3CN.

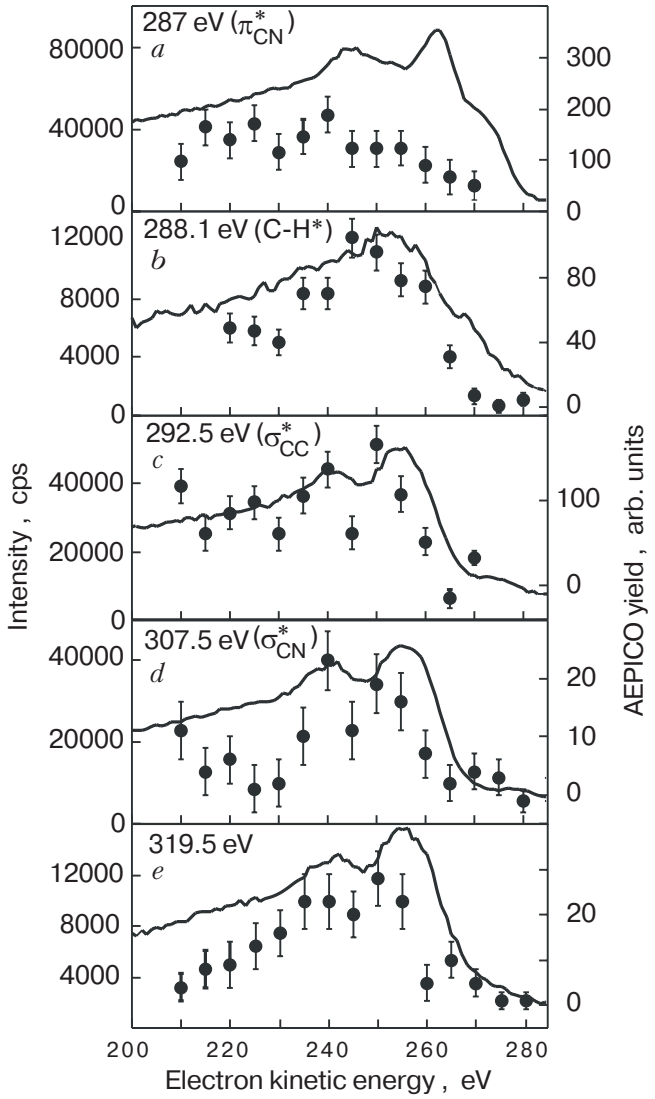

Fig. 20. H^+ AEPICOYS (solid circles) and AES (solid lines) for the C:KVV spectator and normal Auger transitions of condensed CH_3CN.

heavier ionic species to be more effective than for H^+, because of these species' large mass and slow exit velocity [84–86].

Figure 20 shows a series of H^+ AEPICOYS (solid circles) together with the AES (solid lines). At the π^*_{CN} ← C:1*s* resonance (Fig. 20,*a*), in comparison with the spectator AES, the H^+ desorption is suppressed at the peak located at 262 eV. This peak corresponds to the spectator Auger final state in which two holes are formed in the 2*e*, $7a_1$, or 1*e* orbitals [38]. The 2*e* and $7a_1$ electrons do not contribute to the C–H bonding. The initially excited electron occupies the π^*_{CN} orbital, which is mainly distributed over the CN bonding and unrelated to the CH_3 group. The π^*_{CN} electron reduces the hole-hole repulsion due to the shielding effect, so that H^+ desorption is suppressed. At the σ^*_{CC} ← C:1*s* resonance (Fig. 20,*c*), in comparison with the spectator AES, the AEPICOYS is enhanced near 250 eV, which corresponds to the energy of the $(1e)^{-2}(\sigma^*_{CC})^1$ and $(1e)^{-1}(6a_1)^{-1}(\sigma^*_{CC})^1$ spectator Auger final states [38]. The H^+ desorption from the Auger final states with one or two holes in the 1*e* orbital is enhanced. This effect is attributed to the removal of electrons from the C–H bond. At the C–H* ← C:1*s* resonance (Fig. 20,*b*), the AEPICOYS is also enhanced at the $(1e)^{-2}(C–H^*)^1$ and $(1e)^{-1}(6a_1)^{-1}(C–H^*)^1$ states. This is because in these states the excited electron is in the antibonding C–H* orbital and one or two holes are occupied by the pseudo-π_{CH3} 1*e* orbital.

In summary, the electron excitation to the C–H* antibonding orbital and the removal of the electron from the pseudo-π_{CH3} orbital (1*e*) both enhance H^+ ion desorption. On the other hand, electron excitation

to an orbital irrelevant to the C–H bonding suppresses H^+ desorption. Further investigation is needed to determine the predominant H^+ desorption mechanism.

3.4. Site-specific fragmentation of CF_3CH_3

The core electrons of atoms in molecules are localized at their atoms of origin, and the chemical shift shown by an atom depends on the chemical environment of that atom. Like atoms in different chemical environments thus show different chemical shifts. For almost 20 years these properties have been used to study site-specific fragmentation [13,42,91–95], which is potentially useful for controlling chemical reactions through selective bond dissociation. Site-specific fragmentation also offers the possibility of analyzing the structures and properties of molecules, molecular assemblies, and nanoscale devices by controlling matter at the level of individual atoms. To develop these exciting prospects, we need to understand what controls behavior at the atomic level.

Since the chemical shifts of like atoms in a molecule differ site-by-site when the atoms are in different chemical environments, the photoelectron spectrum of the core electrons of those atoms is expected to show a number of peaks equal to the number of different kinds of sites in which the atoms are found. The normal Auger transition caused by photoelectron emission produces two valence holes in molecular orbitals that have a large probability density on the core-ionized atomic site (that is, the Auger transition is localized), and these holes weaken the chemical bonds to which the molecular orbitals are related. Since these molecular orbitals with valence holes have a large probability density on the core-ionized atom, the valence holes weaken the bonds to the core-ionized atom. As a result, site-specific fragmentation occurs at the core-ionized atomic site. The molecule thus «memorizes» the site of the initial energy deposition [96]. To observe a site-specific fragmentation process, we should selectively detect fragments produced by an energy-selected photoelectron emission that corresponds to one of the peaks in the photoelectron spectrum of the core electrons.

S.N. and his collaborators have studied the site-specific fragmentation caused by core-level photoionization of vaporized molecules [42,97–99] and molecules condensed or adsorbed on surfaces [23,41–45,53]. They found that this fragmentation is often better studied on a surface than in a vapor [41–44]. The advantages of EICO experiments on surfaces were explained in Sec. 1.

In this section, we explain the site-specific fragmentation caused by the C:1*s* photoionization of CF_3CH_3 (1,1,1-trifluoroethane, TFEt) condensed on a Au surface [44]. TFEt is the simplest organic molecule with two carbon sites in different chemical environments; one of the carbon atoms is bonded to three hydrogen atoms (C[H]), while the other is bonded to three fluorine atoms (C[F]). Accordingly, TFEt is suitable for such a study because it is a prototypical example of a molecule exhibiting site-specific fragmentation.

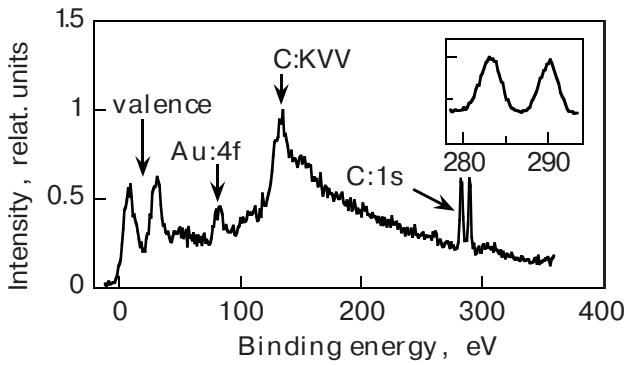

Fig. 21. PES of condensed TFEt, taken at a photon energy of 393.4 eV. The inset shows the range of the C:1*s* electron emission with an enlarged horizontal scale.

Figure 21 shows the PES of TFEt condensed on a Au surface. The peak assignments in the figure were inferred by comparison with the PES and AES of C and Au [100,101]. The PES has two peaks in the range of the C:1*s* electron emission. The low-energy and high-energy peaks were respectively assigned to the C[H]:1*s* and C[F]:1*s* electron emissions based on comparison with the zero-kinetic-energy photoelectron-yield spectrum [96] and the PES [102] of TFEt vapor. The PES of condensed TFEt thus clearly shows that the chemical shifts (binding energies) at the two carbons are different.

The site-specific fragmentation caused by the C:1*s* core-level photoionization of TFEt can be observed by using the PEPICO technique. Figure 22 shows PEPICO spectra obtained with emission of the C[H]:1*s* and C[F]:1*s* electrons. The intensity of the PEPICO signal is proportional to the ion desorption yield measured for a selected electron emission. H^+, CH_3^+, and CF_3^+ ions are desorbed coincidentally with the C[H]:1*s* electrons (Fig. 22,*a*), and $C_2H_n^+$ and $CFCH_m^+$ ions are additionally desorbed with the C[F]:1*s* electrons (Fig. 22,*b*). These PEPICO spectra are very different from the mass spectrum obtained by electron impact in the vapor phase [103]. It should be noted that the C[F]:1*s* ionization induces the desorption of $C_2H_n^+$ and $CFCH_m^+$, both of which contain a C–C bond, but that its desorption is negligible in the C[H]:1*s* ionization. In contrast, H^+, CH_3^+, and CF_3^+, which do not contain a C–C bond, are desorbed with not only the C[F]:1*s* electrons but also the

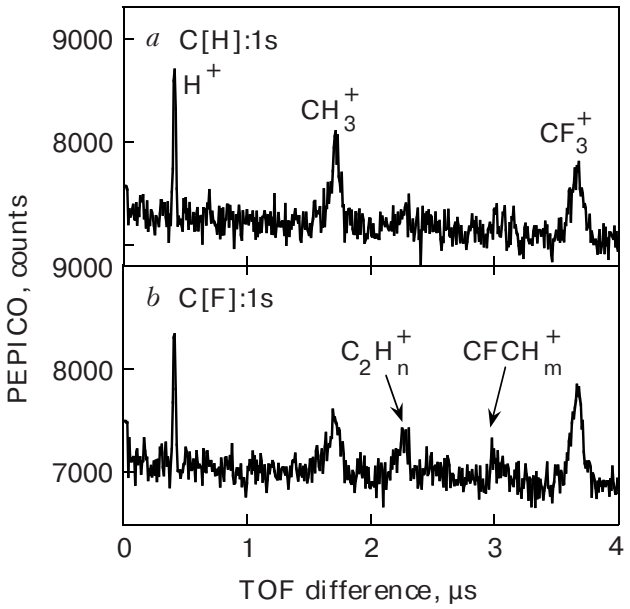

Fig. 22. PEPICO spectra of condensed TFEt, taken at a photon energy of 393.4 eV. (*a*) C[H]:1*s* electron emission, (*b*) C[F]:1s electron emission.

C[H]:1*s* electrons. The intensity ratios of the coincidental desorption with the C[H]:1*s* electron to that with the C[F]:1*s* electron are 1.1 for H^+, 1.2 for CH_3^+, and 0.8 for CF_3^+. The predominant production of CH_3^+ caused by the C[H]:1*s* photoionization is also observed in the normal AEPICO spectrum [44].

Although the site-specificity for H^+, CH_3^+, and CF_3^+ in TFEt is less remarkable than expected from results obtained for condensed $F_3SiCH_2CH_2Si(CH_3)_3$ [41], the predominant fragmentation processes caused by the C[H]:1*s* and C[F]:1*s* photoionizations are as follows.

C[H]:1*s* ionization:

$$\text{TFEt} + h\nu \rightarrow \text{TFEt}^{2+} + 2e \qquad (1a)$$

(photoionization and normal Auger process),

$$\rightarrow H^+ + \text{n.p.}\ , \qquad (1b)$$

$$\rightarrow CH_3^+ + \text{n.p.} \qquad (1c)$$

C[F]:1*s* ionization:

$$\text{TFEt} + h\nu \rightarrow \text{TFEt}^{2+} + 2e \qquad (2a)$$

(photoionization and normal Auger process),

$$\rightarrow CF_3^+ + \text{n.p.}\ , \qquad (2b)$$

$$\rightarrow CFCH_m^+ + \text{n.p.}\ , \qquad (2c)$$

$$\rightarrow C_2H_n^+ + \text{n.p.}\ (n \le m \le 3), \qquad (2d)$$

where n.p. stands for «neutral product». It is assumed that the normal ASID mechanism also plays an important role for TFEt.

The C[H]:1*s* ionization induces the breaking of the C–H bonds (reaction (1b)) and the C–C bond (reaction (1c)), while the C[F]:1*s* ionization induces the breaking of the C–C bond (reaction (2b)) and the C–F bonds (reactions (2c) and (2d)). Thus, site-specific fragmentation occurs around the carbon atom where the photoionization has taken place. The KVV normal Auger transition is localized, and energy randomization destroying the memory of the ionization process does not take place extensively before fragmentation. TFEt moderately memorizes the site of the initial energy deposition, exhibiting the chemical memory effect [96].

Although a strong effect from the site of the initial energy deposition is observed for the fragments $C_2H_n^+$ and $CFCH_m^+$ released from TFEt, the site-specificity for H^+, CH_3^+, and CF_3^+ is, as mentioned above, less remarkable than that previously shown for condensed $F_3SiCH_2CH_2Si(CH_3)_3$ [41]. We cannot yet explain the fragmentation processes for CF_3^+ in the C[H]:1*s* ionization and for H^+ and CH_3^+ in the C[F]:1*s* ionization, but the lesser degree of site-specificity for H^+, CH_3^+, and CF_3^+ in TFEt is thought to be caused by the proximity of the two carbon sites to each other. In fact, we previously showed that site-specificity in $X_3Si(CH_2)_nSi(CH_3)_3$ (X = F or Cl, n = 0–2) decreases with decreasing distance between the two silicon sites [43]. We previously mentioned that site-specific fragmentation is potentially useful for controlling chemical reactions through selective bond dissociation. The present results, however, as well as those for $X_3Si(CH_2)_nSi(CH_3)_3$ (X = F or Cl; n = = 0–2) [43], show that for this process to work well, the atomic site of interest must be far from any atomic site at which bond dissociation is undesirable.

Müller-Dethlefs and his collaborators investigated site-specific fragmentation by studying the ionic fragmentation processes caused by the C:1*s* photoionization of TFEt in the vapor phase [92,96]. The experimental results on the site-specific fragmentation of TFEt were compared with theoretical predictions [104]. The presence of different chemical shifts (different binding energies) that were obtained for TFEt on the surface in the present work is consistent with that obtained for the vapor phase [92,96]. However, the site-specific fragmentation products of TFEt on the surface and in the vapor phase are very different from each other (Table). In the vapor phase, the ionic fragments CFH_2^+, $CF_2CH_2^+$, CF_3^+, C^+, and CF^+ were the most sensitive to the site of the initial energy deposition [96]: the C[H]:1*s* ionization led to

much higher counts of CFH_2^+ and $CF_2CH_2^+$ than did the C[F]:1*s* ionization. The C[H]:1*s* ionization or excitation enhanced the production of CF_3^+, whereas the C[F]:1*s* ionization or excitation enhanced the production of C^+ and CF^+. The C–C bond of the TFEt vapor was more easily broken by C[F]:1*s* ionization or excitation than by C[H]:1*s* ionization or excitation. The fragmentation products of condensed TFEt, in contrast, show that $C_2H_n^+$ and $CFCH_m^+$ are the most sensitive to the site of the initial energy deposition (Fig. 22). Of the fragments whose signals are evident in the spectra of Fig. 22, only $C_2H_n^+$ and $CFCH_m^+$ have a C–C bond, and those ions are desorbed site-specifically after the C[F]:1*s* ionization. The C–C bond in TFEt on the surface is thus more easily broken by C[H]:1*s* ionization than by C[F]:1*s* ionization. In contrast to what was observed for the vapor phase, CF_3^+ is the predominant product of desorption induced by C[F]:1*s* ionization on the surface (reaction (2b)).

Table

Site-specific fragmentation products of TFEt

Condensed TFEt (this work)		TFEt vapor [96]
C[H]:1*s*	H^+, CH_3^+	CFH_2^+, $CF_2CH_2^+$,[a] CF_3^+
C[F]:1*s*	$C_2H_n^+$,[a] $CFCH_m^+$,[a] CF_3^+	C^+, CF^+

Comment: [a] Fragment with a C–C bond.

We do not know exactly why the site-specific fragmentation of TFEt on the surface differs from that of TFEt in the vapor phase, but we can suggest a possible explanation. Tinone et al. [105] previously noted that the reneutralization path is less probable in the vapor phase, all the ions produced are collected by the ion detection apparatus, and the resulting spectrum is an average of all fragmentation paths. For excitation on a solid surface, however, the ions produced through the fast and energetic path are detected selectively. The above-mentioned difference in fragmentation process between TFEt vapor and condensed TFEt may also originate from the difference suggested by Tinone et al.

4. Conclusions and future perspective

In this article we have described the present status of the EICO apparatus and six recent investigations of condensed H_2O, NH_3, CH_3CN, and CF_3CH_3 (site-specific fragmentation) at low temperature. The EICO method is thus a very powerful tool for studies of PSID.

Although condensed molecules are important targets in low temperature physics, a monolayer of a molecule adsorbed on a well-defined surface is more advantageous as a target of EICO studies [22,31,45,49–51]. Judging from this viewpoint, a half monolayer of H_2O or NH_3 adsorbed on H_2O/Si(100) would be interesting. Since H_2O is dissociatively chemisorbed to form Si–OH and Si–H species on Si(100) [64], H_2O and NH_3 are expected to be adsorbed on the Si–OH sites through an intermolecular hydrogen bond, forming a good model for the uppermost molecular layer of the condensed molecules with intermolecular hydrogen bonds. For condensed molecules without intermolecular hydrogen bonds, hydrogen-terminated Si(111) may be an adequate substrate.

An interesting subject for future work would be development of advanced coincidence apparatus. EICO spectroscopy using a reflectron TOF-MS [106] would be useful for the study of polymer surfaces. Coincidence between an electron and an energy-selected-ion will offer information on the potential energy surface responsible for PSID. Coincidence between an electron and an angle-resolved-ion will clarify the configuration of the surface species responsible for PSID. By using photoelectron–Auger-electron–photoion triple coincidence spectroscopy, one would be able to directly connect the photoionization initial state, the Auger final state, and the resultant ion desorption. Coincidence between a photoelectron (or an Auger electron) and a photon emitted from a neutral fragment would also be interesting. Although neutral species are not easily detected by ordinary methods, detection of their photon emission would not be very difficult. EICO spectroscopy combined with vacuum ultraviolet light, hard x-ray, electron beam, ion beam, multiply-charged ion beam, energetic neutral beam, metastable atom beam, positron beam, and so on is prospective fields. EICO spectroscopy is also hopeful as a surface analysis technique, because EICO spectra can be used as high sensitive PES and AES (Sec. 3.1.2), and because EICO spectroscopy can detect a surface hydrogen atom and can specify the atom to which a desorbed ion is bonded. The coincidence method is a promising method for further studies of surface science.

5. Acknowledgments

The «we» in this paper is not necessarily synonymous with only K.M., M.N., S.T., T.S., and S.N., but also represents contributions from various combinations of the authors' collaborators. Their contributions are greatly acknowledged. We also express our sincere thanks to the members of the UVSOR and PF synchrotron radiation facilities for their valuable help during the course of the experiments.

1. T.E. Madey, *Surf. Sci.* **299/300**, 824 (1994).
2. D.E. Ramaker, in: *Desorption Induced by Electronic Transitions*, DIET-II, Vol. 4 of Springer Series in Surface Sciences, W. Brenig and D. Menzel (eds.) Springer, Berlin (1985), p. 10.
3. V. Rehn and R.A. Rosenberg, in: *Synchrotron Radiation Research: Advances in Surface and Interface Science*, Vol. 1, R.Z. Bachrach (ed.) Plenum, New York (1992), p. 327.
4. R.A. Rosenberg and V. Rehn, in: *Synchrotron Radiation Research: Advances in Surface and Interface Science*, Vol. 2, R.Z. Bachrach (ed.) Plenum Press, New York (1992), p. 267.
5. R. Treichler, W. Wurth, W. Riedl, P. Feulner, and D. Menzel, *Chem. Phys.* **153**, 259 (1991).
6. R.A. Rosenberg and S.P. Frigo, in: *Chemical Applications of Synchrotron Radiation Part I: Dynamics and VUV Spectroscopy*, T.-K. Sham (ed.) World Scientific, Singapore (2002), p. 462.
7. T.E. Madey, R.E. Johnson, and T.M. Orlando, *Surf. Sci.* **500**, 838 (2002).
8. M.T. Sieger, W.C. Simpson, and T.M. Orlando, *Nature* **394**, 554 (1998).
9. B.V. Yakshinskiy and T.E. Madey, *Nature* **400**, 642 (1999).
10. D.A. Williams, in: *Dust and Chemistry in Astronomy*, D.A. Williams and T.J. Millar (eds.), IOP Publishing, Philadelphia (1993), p. 143.
11. E. Herbst, *Annu. Rev. Phys. Chem.* **46**, 27 (1995).
12. D.E. Ramaker, T.E. Madey, R.L. Kurtz, and H. Sambe, *Phys. Rev.* **B38**, 2099 (1988).
13. R. Romberg, N. Heckmair, S.P. Frigo, A. Ogurtsov, D. Menzel, and P. Feulner, *Phys. Rev. Lett.* **84**, 374 (2000).
14. P. Feulner, R. Romberg, S.P. Frigo, R. Weimar, M. Gsell, A. Ogurtsov, and D. Menzel, *Surf. Sci.* **451**, 41 (2000).
15. R. Weimar, R. Romberg, S.P. Frigo, B. Kassühlke, and P. Feulner, *Surf. Sci.* **451**, 124 (2000).
16. *VUV and Soft X-Ray Photoionization*, U. Becker and D.A. Shirley (eds.) Plenum Press, New York (1996) and references cited therein.
17. R. Murphy and W. Eberhardt, *J. Chem. Phys.* **89**, 4054 (1988).
18. W. Eberhardt, E.W. Plummer, I.-W. Lyo, R. Carr, and W.K. Ford, *Phys. Rev. Lett.* **58**, 207 (1987).
19. M.L. Knotek and J.W. Rabalais, in: *Desorption Induced by Electronic Transitions*, DIET-II, Vol. 4 of Springer Series in Surface Sciences, W. Brenig and D. Menzel (eds.) Springer, Berlin (1985), p. 77.
20. K. Mase, M. Nagasono, T. Urisu, and Y. Murata, *Bull. Chem. Soc. Jpn.* **69**, 1829 (1996).
21. K. Mase, M. Nagasono, S. Tanaka, M. Kamada, T. Urisu, and Y. Murata, *Rev. Sci. Instrum.* **68**, 1703 (1997).
22. K. Mase and S. Tanaka, *Jpn. J. Appl. Phys. Suppl.* **38–1**, 233 (1999).
23. K. Mase, S. Tanaka, S. Nagaoka, and T. Urisu, *Surf. Sci.* **451**, 143 (2000).
24. K. Mase, *Kanae*, **13**, 18 (2000) (in Japanese).
25. K. Isari, K. Tanaka, S. Nagaoka, T. Gejo, H. Yoshida, and K. Mase, *J. Vac. Soc. Jpn.* (in Japanese), *in press*.
26. K. Isari, E. Kobayashi, K. Mase, and K. Tanaka, *Surf. Sci.*, *in preparation*.
27. M. Nagasono, K. Mase, and T. Urisu, *Surf. Sci.* **363**, 342 (1996).
28. K. Mase, M. Nagasono, S. Tanaka, T. Urisu, E. Ikenaga, T. Sekitani, and K. Tanaka, *Surf. Sci.* **390**, 97 (1997).
29. M. Nagasono, K. Mase, S. Tanaka, and T. Urisu, *Chem. Phys. Lett.* **298**, 141 (1998).
30. K. Mase, M. Nagasono, S. Tanaka, T. Urisu, E. Ikenaga, T. Sekitani, and K. Tanaka, *J. Chem. Phys.* **108**, 6550 (1998).
31. K. Mase, M. Nagasono, and S. Tanaka, *J. Vac. Soc. Jpn.* **42**, 84 (1999) (in Japanese).
32. S. Tanaka, K. Mase, M. Nagasono, S. Nagaoka, M. Kamada, E. Ikenaga, T. Sekitani, and K. Tanaka, *Jpn. J. Appl. Phys.* **39**, 4489 (2000).
33. M. Nagasono, K. Mase, S. Tanaka, and T. Urisu, *Surf. Sci.* **377–379**, 380 (1997).
34. M. Nagasono, K. Mase, S. Tanaka, and T. Urisu, *Surf. Sci.* **390**, 102 (1997).
35. M. Nagasono, K. Mase, S. Tanaka, and T. Urisu, *Jpn. J. Appl. Phys. Suppl.* **38–1**, 325 (1999).
36. T. Sekitani, E. Ikenaga, K. Tanaka, K. Mase, M. Nagasono, S. Tanaka, and T. Urisu, *Surf. Sci.* **390**, 107 (1997).
37. T. Sekitani, E. Ikenaga, H. Matsuo, S. Tanaka, K. Mase, and K. Tanaka, *J. Electron Spectrosc. Relat. Phenom.* **88–91**, 831 (1998).
38. T. Sekitani, E. Ikenaga, K. Fujii, K. Mase, N. Ueno, and K. Tanaka, *J. Electron Spectrosc. Relat. Phenom.* **101–103**, 135 (1999).
39. K. Mase, M. Nagasono, S. Tanaka, T. Urisu, and S. Nagaoka, *Surf. Sci.* **377–379**, 376 (1997).
40. I. Shimoyama, T. Mochida, Y. Otsuki, H. Horiuchi, S. Saijyo, K. Nakagawa, M. Nagasono, S. Tanaka, and K. Mase, *J. Electron Spectrosc. Relat. Phenom.* **88–91**, 793 (1998).
41. S. Nagaoka, K. Mase, M. Nagasono, S. Tanaka, T. Urisu, and J. Ohshita, *J. Chem. Phys.* **107**, 10751 (1997).
42. S. Nagaoka, K. Mase, and I. Koyano, *Trends Chem. Phys.* **6**, 1 (1997).
43. S. Nagaoka, K. Mase, M. Nagasono, S. Tanaka, T. Urisu, J. Ohshita, and U. Nagashima, *Chem. Phys.* **249**, 15 (1999).
44. S. Nagaoka, S. Tanaka, and K. Mase, *J. Phys. Chem.* **B105**, 1554 (2001).
45. S. Nagaoka, K. Mase, A. Nakamura, M. Nagao, J. Yoshinobu, and S. Tanaka, *J. Chem. Phys.* **117**, 3961 (2002).
46. E. Ikenaga, K. Isari, K. Kudara, Y. Yasui, S.A. Sardar, S. Wada, T. Sekitani, K. Tanaka, K. Mase, and S. Tanaka, *J. Chem. Phys.* **114**, 2751 (2001).

47. E. Ikenaga, K. Kudara, K. Kusaba, K. Isari, S.A. Sardar, S. Wada, K. Mase, T. Sekitani, and K. Tanaka, *J. Electron Spectrosc. Relat. Phenom.* **114–116**, 585 (2001).
48. K. Tanaka, E.O. Sako, E. Ikenaga, K. Isari, S.A. Sardar, S. Wada, T. Sekitani, K. Mase, and N. Ueno, *J. Electron Spectrosc. Relat. Phenom.* **119**, 255 (2001).
49. S. Tanaka, K. Mase, M. Nagasono, and M. Kamada, *Surf. Sci.* **390**, 204 (1997).
50. S. Tanaka, K. Mase, S. Nagaoka, M. Nagasono, and M. Kamada, *J. Chem. Phys.* **117**, 4479 (2002).
51. S. Tanaka, K. Mase, M. Nagasono, and M. Kamada, *J. Electron Spectrosc. Relat. Phenom.* **92**, 119 (1998).
52. S. Tanaka, K. Mase, M. Nagasono, S. Nagaoka, and M. Kamada, *Surf. Sci.* **451**, 182 (2000).
53. K. Mase, M. Nagasono, S. Tanaka, and S. Nagaoka, *J. Jpn. Soc. Synchrotron Radiation Res.* **10**, 375 (1997) (in Japanese).
54. K. Mase, M. Nagasono, and S. Tanaka, *J. Electron Spectrosc. Relat. Phenom.* **101–103**, 13 (1999).
55. K. Mase, *Chem. Chem. Ind.* **53**, 111 (2000) (in Japanese).
56. K. Siegbahn, N. Kholine, and G. Golikov, *Nucl. Instrum. Methods* **A384**, 563 (1997).
57. M.L. Knotek and P.J. Feibelman, *Phys. Rev. Lett.* **40**, 964 (1978).
58. R. Franchy and D. Menzel, *Phys. Rev. Lett.* **43**, 865 (1979).
59. D.R. Jennison, J.A. Kelber, and R.R. Rye, *Phys. Rev.* **B25**, 1384 (1982).
60. P.J. Feibelman, *Surf. Sci.* **102**, L51 (1981).
61. M. Cini, *Phys. Rev.* **B32**, 1945 (1985).
62. D.E. Ramaker, C.T. White, and J.S. Murday, *Phys. Lett.* **A89**, 211 (1982).
63. J.P. Devlin and V. Buch, *J. Phys. Chem.* **99**, 16534 (1995).
64. P.A. Thiel and T.E. Madey, *Surf. Sci. Rep.* **7**, 211 (1987).
65. M.A. Henderson, *Surf. Sci. Rep.* **46**, 1 (2002).
66. D.E. Ramaker, *Chem. Phys.* **80**, 183 (1983).
67. M.T. Sieger, W.C. Simpson, and T.M. Orlando, *Phys. Rev.* **B56**, 4925 (1997).
68. R.A. Rosenberg, P.R. LaRoe, V. Rehn, J. Stöhr, R. Jaeger, and C.C. Parks, *Phys. Rev.* **B28**, 3026 (1983).
69. D. Coulman, A. Puschmann, U. Höfer, H.-P. Steinrück, W. Wurth, P. Feulner, and D. Menzel, *J. Chem. Phys.* **93**, 58 (1990).
70. H. Siegbahn, L. Asplund, and P. Kelfve, *Chem. Phys. Lett.* **35**, 330 (1975).
71. H. Ågren, S. Svensson, and U.I. Wahlgren, *Chem. Phys. Lett.* **35**, 336 (1975).
72. P. Morin and I. Nenner, *Phys. Rev. Lett.* **56**, 1913 (1986).
73. M.N. Piancastelli, A. Hempelmann, F. Heiser, O. Gessner, A. Rüdel, and U. Becker, *Phys. Rev.* **A59**, 300 (1999).
74. I. Hjelte, M.N. Piancastelli, R.F. Fink, O. Björneholm, M. Bässler, R. Feifel, A. Giertz, H. Wang, K. Wiesner, A. Ausmees, C. Miron, S.L. Sorensen, and S. Svensson, *Chem. Phys. Lett.* **334**, 151 (2001).
75. R. Romberg, S.P. Frigo, A. Ogurtsov, P. Feulner, and D. Menzel, *Surf. Sci.* **451**, 116 (2000).
76. C. Keller, M. Stichler, G. Comelli, F. Esch, S. Lizzit, W. Wurth, and D. Menzel, *Phys. Rev. Lett.* **80**, 1774 (1998).
77. C. Keller, M. Stichler, G. Comelli, F. Esch, S. Lizzit, D. Menzel, and W. Wurth, *Phys. Rev.* **B57**, 11951 (1998).
78. W. Wurth and D. Menzel, *Chem. Phys.* **251,** 141 (2000).
79. W.F. Egelhoff, Jr., *Surf. Sci. Rep.* **6**, 253 (1987).
80. M. Akbulut, N.J. Sack, and T.E. Madey, *Surf. Sci. Rep.* **28**, 177 (1997).
81. N. Martensson, P.-Å. Malmquist, S. Svensson, E. Basilier, J.J. Pireaux, U. Gelius, and K. Siegbahn, *Nouv. J. Chim.* **1**, 191 (1976).
82. B. Baron and F. Williams, *J. Chem. Phys.* **64**, 3896 (1976).
83. F.P. Larkins and A. Lubenfeld, *J. Electron Spectrosc. Relat. Phenom.* **15**, 137 (1979).
84. R.D. Ramsier and J.T. Yates, Jr., *Surf. Sci. Rep.* **12**, 243 (1991).
85. J.-G. Lee, J. Ahner, and J.T. Yates, Jr., *J. Chem. Phys.* **114**, 1414 (2001).
86. J.-G. Lee, J. Ahner, P. Maksymovych, and J.T. Yates, Jr., *Chem. Phys. Lett.* **340**, 21 (2001).
87. D. Menzel, G. Rocker, D. Coulman, P. Feulner, and W. Wurth, *Phys. Scr.* **41**, 588 (1990).
88. J. Schirmer, A.B. Trofimov, K.J. Randall, J. Feldhaus, A.M. Bradshaw, Y. Ma, C.T. Chen, and F. Sette, *Phys. Rev.* **A47**, 1136 (1993).
89. K. Kimura, S. Katsumata, Y. Achiba, T. Yamazaki, and S. Iwata, *Handbook of He I Photoelectron Spectra of Fundamental Organic Molecules*, Japan Scientific Societies Press/Halsted Press, Tokyo/New York (1981).
90. P.A. Stevens, R.J. Madix, and J. Stöhr, *J. Chem. Phys.* **91**, 4338 (1989).
91. W. Eberhardt, T.K. Sham, R. Carr, S. Krummacher, M. Strongin, S.L. Weng, and D. Wesner, *Phys. Rev. Lett.* **50**, 1038 (1983).
92. K. Müller-Dethlefs, M. Sander, L.A. Chewter, and E.W. Schlag, *J. Phys. Chem.* **88**, 6098 (1984).
93. D.M. Hanson, *Adv. Chem. Phys.* **77**, 1 (1990).
94. N. Ueno and K. Tanaka, *J. Jpn. Soc. Synchrotron Radiation Res.* **9**, 29 (1996) (in Japanese).
95. I. Nenner, C. Reynaud, H.C. Schmelz, L. Ferrand-Tanaka, M. Simon, and P. Morin, *Z. Phys. Chem.* **195**, 43 (1996).
96. W. Habenicht, H. Baiter, K. Müller-Dethlefs, and E.W. Schlag, *J. Phys. Chem.* **95**, 6774 (1991).
97. S. Nagaoka, J. Ohshita, M. Ishikawa, K. Takano, U. Nagashima, T. Takeuchi, and I. Koyano, *J. Chem. Phys.* **102**, 6078 (1995).

98. S. Nagaoka, T. Fujibuchi, J. Ohshita, M. Ishikawa, and I. Koyano, *Int. J. Mass Spectrom. Ion Processes* **171**, 95 (1997).
99. S. Nagaoka, T. Fujibuchi, J. Ohshita, U. Nagashima, and I. Koyano, *Chem. Phys*. **276**, 243 (2002).
100. C.D. Wagner, W.M. Riggs, L.E. Davis, J.F. Moulder, and G. E. Muilenberg, *Handbook of X-ray Photoelectron Spectroscopy*. Perkin-Elmer, Eden Prairie, Minnesota, (1979).
101. K.D. Childs, B.A. Carlson, L.A. LaVanier, J.F. Moulder, D.F. Paul, W.F. Stickle, D.G. Watson, and C.L. Hedberg, *Handbook of Auger Electron Spectroscopy 3rd Edition*, Physical Electronics, Eden Prairie, Minnesota (1995).
102. A.P. Hitchcock, *Phys. Scr*. **T31**, 159 (1990).
103. J.M. Simmie and E. Tschuikow-Roux, *Int. J. Mass Spectrom. Ion Phys*. **7**, 41 (1971).
104. I. Salman, J. Silberstein, and R.D. Levine, *J. Phys. Chem*. **95**, 6781 (1991).
105. M.C.K. Tinone, K. Tanaka, J. Maruyama, N. Ueno, M. Imamura, and N. Matsubayashi, *J. Chem. Phys*. **100**, 5988 (1994).
106. U. Boesl, R. Weinkauf, and E.W. Schlag, *Int. J. Mass Spectrom. Ion Processes* **112**, 121 (1992).